



Published in final edited form as:

Cancer Cell. 2023 August 14; 41(8): 1480–1497.e9. doi:10.1016/j.ccell.2023.06.007.

Tissue factor is a critical regulator of radiation therapy-induced glioblastoma remodeling

Hye-Min Jeon¹, Jeong-yup Kim², Hee-Jin Cho³, Won Jun Lee¹, Dayna Nguyen¹, Sungsoo Kim⁴, Young Taek Oh⁴, Hee-Jin Kim², Chan-Woong Jung², Dolores Hambarzumyan⁵, Takuya Sakaguchi⁶, Christopher Hubert⁷, Thomas M. McIntyre⁸, Howard A. Fine⁹, Candace L. Gladson¹, Bingcheng Wang¹⁰, Benjamin W. Purow¹¹, Jong Bae Park⁴, Myung Jin Park², Do-Hyun Nam¹², Jeongwu Lee^{1,13,*}

¹Department of Cancer Biology, Lerner Research Institute, Cleveland Clinic, Cleveland, OH, USA

²Divisions of Radiation Cancer Research, Research Center for Radio-Senescence, Korea Institute of Radiological and Medical Sciences, Seoul, Korea.

³Department of Biomedical Convergence Science and Technology, Kyungpook National University, Daegu, Korea.

⁴Department of System Cancer Science, Graduate School of Cancer Science and Policy, National Cancer Center, Goyang, Korea.

⁵Icahn School of Medicine at Mount Sinai, New York, NY, USA.

⁶Department of Inflammation and Immunity, Lerner Research Institute, Cleveland Clinic, Cleveland, OH, USA

⁷Department of Biomedical Engineering, Lerner Research Institute, Cleveland Clinic, Cleveland, OH, USA

⁸Department of Cardiovascular and Metabolic Sciences, Lerner Research Institute, Cleveland Clinic, Cleveland, OH, USA.

⁹Department of Neurology, Weill Cornell Medicine, New York, NY, USA.

¹⁰Department of Medicine, MetroHealth Campus, School of Medicine, Case Western Reserve University, Cleveland, OH, USA.

*Correspondence to: Jeongwu Lee, leej7@ccf.org.

AUTHOR CONTRIBUTIONS

Conceptualization: H-M.J. and J.L.; Methodology: H-M.J., D.H., M.L.B., S.W., A.M.J., S.N., A.J.N., R.K.; Investigation: H-M.J., J-Y.K., H-J.C., S.K., Y.T.O., H-J.K., C-W.J., and T.S.; Validation: H-M.J., J-Y.K., and H-J.C.; Formal Analysis: H-M.J., D.N., W.J.L., and H-J.C.; Resources: H.A.F., B.W., C.H., D.H., J.B.P., M.J.P., T.J., D-H. N, and J.L.; Data Curation: H-M.J., H-J. C., W.J.L., D.N. and T.S.; Writing–Original Draft: H-M. J., B.W.P., and J.L.; Writing–Reviewing & Editing: H-M. J., B.W.P., T.M.M., C.L.P., and J.L.; Supervision: J.B.P., M.J.P., D-H. N, and J.L.; Project Administration: J.L.; Funding Acquisition: J.L.

DECLARATION OF INTERESTS

H-M.J. and J.L. are co-inventors on a filed patent application for the use of truncated F7 recombinant protein to treat cancer.

Publisher's Disclaimer: This is a PDF file of an unedited manuscript that has been accepted for publication. As a service to our customers we are providing this early version of the manuscript. The manuscript will undergo copyediting, typesetting, and review of the resulting proof before it is published in its final form. Please note that during the production process errors may be discovered which could affect the content, and all legal disclaimers that apply to the journal pertain.

¹¹Department of Neurology, UVA Cancer Center, University of Virginia Health System, Charlottesville, VA, USA.

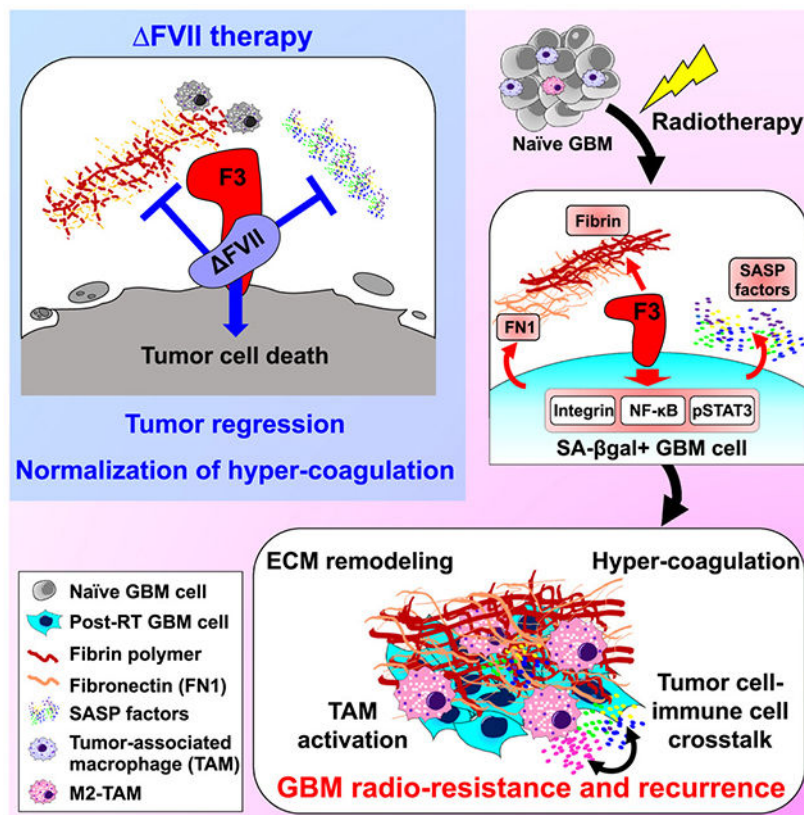
¹²Institute for Refractory Cancer Research, Samsung Medical Center; Department of Health Sciences and Technology, Samsung Advanced Institute for Health Sciences and Technology; Department of Neurosurgery Samsung Medical Center, Sungkyunkwan University School of Medicine, Seoul, Korea.

¹³Lead contact

Summary

Radiation therapy (RT) provides therapeutic benefit for patients with glioblastoma (GBM), but inevitably induces poorly-understood global changes in GBM and its microenvironment (TME) that promote radio-resistance and recurrence. Through a cell surface marker screen, we identified that CD142 (Tissue factor or F3) is robustly induced in the senescence-associated β -galactosidase (SA- β Gal)-positive GBM cells after irradiation. F3 promotes clonal expansion of irradiated SA- β Gal⁺ GBM cells and orchestrates oncogenic TME remodeling by activating both tumor-autonomous signaling and extrinsic coagulation pathways. Intratumoral F3 signaling induces a mesenchymal-like cell state transition and elevated chemokine secretion. Simultaneously, F3-mediated focal hypercoagulation states lead to activation of tumor-associated macrophages (TAMs) and extracellular matrix (ECM) remodeling. A newly developed F3-targeting agent potently inhibits the above oncogenic events and impedes tumor relapse *in vivo*. These findings support F3 as a critical regulator for therapeutic resistance and oncogenic senescence in GBM, opening potential therapeutic avenues.

Graphical Abstract



eTOC

Jeon et al. find that Tissue factor (F3) is robustly upregulated in irradiated glioblastoma (GBM) cells. F3 signaling promotes irradiation-induced global remodeling of GBM tumor and its microenvironment, leading to GBM radio-resistance and recurrence. A new F3-targeting agent potently inhibits the above oncogenic events and impedes tumor relapse *in vivo*.

Keywords

Glioblastoma; Tissue factor; Senescence; Therapeutic resistance; Tumor microenvironment

Introduction

Glioblastoma (GBM) is the most lethal brain cancer with no curative therapies available. Recent anti-angiogenic and immunotherapy approaches have not yet shown durable clinical benefits for GBM patients^{1,2}. Currently, maximal surgical resection followed by radiation therapy (RT) and temozolomide (TMZ) chemotherapy is standard-of-care therapy for newly diagnosed GBM patients³. Limited benefits from current therapies can be attributed to multiple factors, including inherent radio-resistance of GBM tumors, preferential survival of GBM stem-like cells, and treatment-induced activation of pro-tumorigenic adaptive pathways⁴⁻⁶.

RT exerts cytostatic and cytotoxic anti-tumor effects against GBM, but tumor relapse is almost inevitable. Following RT, GBM tumors undergo phenotypic transition via global remodeling of epigenetic and transcriptome landscapes. RT enhances the secretion of various chemokines, cytokines, and extracellular matrix (ECM) molecules by tumor cells^{7,8}. Many of RT-induced chemo/cytokines are known to induce GBM cell state transition and mediate reciprocal crosstalk between GBM cells and immune cells^{9–11}. In addition, RT is a potent inducer of coagulopathy and immune modulation^{12–14}. While the above RT-induced global changes have long been hypothesized to account for tumor evolution and aggressiveness of recurrent tumors, the upstream initiators of these processes are poorly understood.

In many malignant tumors such as GBM, irradiation and targeted inhibitors transiently induce tumor cell senescence, referred to as therapy-induced senescence (TIS)^{15,16}. Because the senescence program involves global epigenomic reprogramming and the elevated secretion of multiple proteins, referred to as the senescence-associated secretory phenotype (SASP), TIS may play a role in RT-induced global changes^{17,18}. Tumor cell senescence remains poorly defined, with key questions unanswered including how senescent tumor cell states are regulated and how TIS affects treatment resistance and tumor recurrence. Here, we used an integrative approach to understand tumor cell senescence in the course of radiation resistance, combining the assays with a modified senescence-associated β -galactosidase (SA- β Gal) substrate that allows sorting and live cell fate tracing of the senescent tumor cells, cell surface marker screening, single cell RNA sequencing, and profiling of transcriptome and chromatin landscapes. We demonstrate a causal link between RT-induced senescence and global oncogenic reprogramming and derive new therapeutic strategy to inhibit these processes.

Results

Irradiation-induced SA- β Gal⁺ GBM cells harbor stemness and senescence-like features.

To determine the extent of senescence in GBM tumor, we utilized three different orthotopic patient-derived GBM models (Figure 1A). 827 and 022 GBM cells have homozygous deletion of *Cdkn2a*, a common genomic alteration found in GBM¹⁹. The brains of tumor-bearing mice were irradiated and the activity of SA- β Gal were measured with either a colorimetric substrate X-Gal or a cell-permeable fluorogenic substrate C₁₂FDG^{20,21} (Figures 1A and S1A). Irradiation induced strong SA- β Gal activity especially in the tumor regions (Figure 1A). To determine the cell types of SA- β Gal⁺ cells, we implanted red fluorescent protein (RFP)-transduced GBM tumors, irradiated the mice *in vivo*, and stained with C₁₂FDG (Figure 1B). Flow cytometry analysis revealed that more than 90 % of SA- β Gal⁺ cells in the irradiated brains were positive for RFP, indicating that primarily GBM cells acquire RT-induced SA- β Gal activity (Figure 1B). To better cover inter-tumoral GBM genetic heterogeneity and to avoid model-dependent biases, we utilized multiple patient-derived GBM slices and organoids (Details are in Method sections)^{22–24}. Across all GBM samples tested, we found robust induction of SA- β Gal activity after RT (Figure S1 B and C).

To investigate cellular states of post-irradiated SA- β Gal⁺ GBM cells, we separated SA- β Gal⁺ and SA- β Gal⁻ GBM subpopulations by C₁₂FDG staining and subsequent

fluorescence-activated cell sorting (FACS). DNA damage repair activity and clonal growth capacity are critical for GBM radio-resistance and subsequent recurrence⁴. C₁₂FDG⁺ cells after irradiation (RT-C₁₂FDG⁺) showed enhanced activities of ATM and DNA checkpoint kinases, relative to matched C₁₂FDG^{low/-} or mock-sorted bulk tumor cells (Figure 1C). Furthermore, RT-C₁₂FDG⁺ cells expressed Nestin (a representative GBM stemness marker) and were highly enriched with clonogenic cells, as determined by *in vitro* colony forming analysis (Figure 1D and E). Next, we determined the levels of representative senescence markers in GBM tumors with or without irradiation. RT-C₁₂FDG⁺ cells had high levels of HP1 and H3K9me3 but little or no expression of CDKN2A (also known as p16, a cell-cycle arrest-associated senescence marker) (Figure 1F to I and data not shown). Notably, RT increased the number of GBM cells that express both Nestin and H3K9me3, which were further enriched in RT-C₁₂FDG⁺ cells (Figure 1G).

To examine global transcriptomes of SA-βGal⁺ GBM cells, we performed single-cell RNA sequencing (scRNA-seq) and bulk RNA seq analysis. In total, we profiled about 100,000 single GBM cells and classified these cells based on the expression levels of stemness and cell cycle progression^{25–27}. Both naïve and irradiated GBM cells contained the cell populations with high expression levels of the cell cycle and/or stemness gene signatures, reflecting their aggressive nature. Notably, RT-C₁₂FDG⁺ subpopulation harbored most of the single cells that have the highest scores for the stemness gene signature (Figures 1H and I).

Cellular senescence has been extensively studied in irradiated IMR90 or WI38 cells (non-transformed human fibroblasts). Consistent with a traditional view of senescence, SA-βGal⁺ IMR90 or WI38 cells did not proliferate (Figure S1D and E). In contrast, bulk RNA sequencing analysis of matched C₁₂FDG⁺ and C₁₂FDG^{low/-} GBM cells after radiation showed that many of the cell cycle signature genes, including *PCNA*, *BUB1*, and *FoxM1* are highly expressed in C₁₂FDG⁺ cells^{28,29} (Figure S1F to H). These data suggest that SA-βGal⁺ GBM cells do not exhibit the irreversible cell cycle arrest state.

To formally test whether RT-SA-βGal⁺ GBM cells can clonally expand and contribute to post-RT tumor growth, we used the lentiviral-mediated barcode/RFP transduction technology to label GBM cells. We isolated C₁₂FDG⁺ cells from the irradiated, labeled GBM tumors and immediately injected these cells into the brains of new recipient mice (Figure 1J to M). RT-C₁₂FDG⁺ GBM cells generated significantly larger tumors in new recipient mice, compared to non-irradiated (naïve) or irradiated bulk tumor cells (Figure 1K). Clonal expansion analysis by barcode sequencing revealed that larger numbers of individual barcodes were detected in the tumors derived from RT-C₁₂FDG⁺ GBM cells compared to those of naïve or RT-bulk cells (Figure 1L). This trend corroborates well with the current notion of the clonal diversity in cancer following treatment^{30,31}. Lastly, we performed *in vivo* limiting dilution tumor formation assays using the above cell populations. RT-C₁₂FDG⁺ cells derived from two different patient GBMs contained higher frequencies of tumor-forming cells than RT-bulk- or C₁₂FDG⁻ cells (Figure 1M). Collectively, these data suggest that irradiation-induced SA-βGal⁺ GBM cells harbor stemness and some of senescence-like characteristics and that they are a cell population contributing to post-RT tumor growth.

F3, highly expressed in irradiated C₁₂FDG⁺ GBM cells, is associated with stemness, cell state transition, and an enhanced secretory phenotype.

To investigate cellular states and molecular regulators of SA-βGal⁺ GBM cells, we profiled levels of cell surface proteins. Matched naïve and irradiated GBM cells (20 million cells each) were stained with C₁₂FDG, split into individual wells, and co-stained with each of 242 human clusters of differentiation (CD) antibodies (Figure 2A). Co-staining results were quantitated by flow cytometry and expression level of each CD marker was calculated. Enriched cell surface receptors in RT-C₁₂FDG⁺ cells included ABCG2, JAMA, PDGFR, CD109 and integrin proteins, implicated in stemness, GBM mesenchymal transition, and therapeutic resistance (Figure 2B)^{32–34}. The most enriched CD marker in our screen was CD142 (Tissue factor or F3), originally identified as a cell surface receptor that initiates blood coagulation³⁵. Tissue factor/F3 levels were increased over 10-fold in irradiated cells compared to the matched naïve cells, further increased in RT-C₁₂FDG⁺ cells (Figure 2B). In the irradiated PDX tumor-bearing mice, we found the robust F3 induction, co-localized with C₁₂FDG⁺ tumor cells (Figure 2C). This trend was further confirmed in GBM spheroids, GBM organoids and patient GBM slices (Figure S2 A to G).

Two F3 canonical functions are initiation of blood coagulation and promotion of cell survival via intracellular signaling. Coagulation factor VII (F7, a cognate F3 ligand) is mainly produced in the liver and circulates in the blood stream as an inactive pro-enzyme. Upon interaction with F3, F7 is converted into a protease-active form (FVIIa), which then initiates coagulation by catalyzing a thrombin-producing protease cascade^{36,37}. Intracellular signaling is mediated by activation of integrin and the protease-activated receptor (PAR), leading to activation of MAPK, PI3K, and NFκB^{38,39}. While F3 is expressed in various tumor types—including gliomas—and generally exerts pro-tumor effects^{40–42}, the role(s) of F3 in RT responses and senescence are largely unknown.

To test whether post-irradiated F3^{high} cells are enriched for *in vivo* tumorigenic capacity, we isolated matched F3^{high} and F3^{low/-} cells from PDX tumors 5 days after *in vivo* radiation by F3 antibody-based cell sorting, and then injected these cells into immunodeficient mice. Compared to matched F3^{low/-} or mock-sorted bulk tumor cells, post-irradiated F3^{high} subpopulations yielded significantly higher capacities for tumor formation (Figure 2 D and E).

To gain insight into signaling nodes associated with F3, we performed ATAC (assay for transposase-accessible chromatin)-seq analysis to map genome regions with open chromatin structures in matched F3^{high} and F3^{low/-} subpopulations. The most enriched transcription factor-binding motifs in RT-F3⁺ GBM cells are STAT3 and FOSL2 (master transcriptional factors for the GBM mesenchymal (MES) transcriptional network), RELA (NFκB, a master regulator for senescence and GBM cell survival), as well as Foxo4 and TEAD2 (implicated in tumor dormancy and senescence)^{43–46}, most of which were also enriched in RT-C₁₂FDG⁺ GBM cells (Figures 2F and S2I). Following RT, GBM tumors undergo phenotypic transition toward MES subtype, which is mediated by activation of NFκB and STAT3 signaling^{9,45}. We then determined the activation status of these pathways by immunoblots, immunostaining, and transcriptome analysis (Figures 2 G to L and S2 A to K). Consistent with ATAC data, irradiated F3^{high} GBM cells have elevated levels of

active NF κ B and STAT3 as well as stemness-associated proteins (Sox2, EZH2, and active β -catenin and integrin β 1^{47,48} (Figures 2 G and H, and S2 H to K). Active integrin signaling in this subpopulation is further supported by additional surface marker screening using anti-F3 antibody and 240 human CD markers. Similar to the C₁₂FDG co-staining data, several different integrin family proteins were highly enriched in irradiated F3^{high} GBM cells (Table S1). In addition, RT-F3⁺ cells have high levels of GBM mesenchymal markers (YKL-40, CD44, and active STAT3) (Figures 2J, 2K and S2J)⁴⁹. Lastly, secretome profiling and gene signature analysis showed that irradiated F3^{high} GBM cells secreted significantly higher levels of SASP factors such as IL6, IL8, HGF, and EGF, relative to bulk naïve or irradiated tumor cells (Figure 2 L and M). Together, these data indicate that the RT-F3⁺ populations have enriched traits of stemness, mesenchymal GBM cell transition, senescence-like epigenomic reprogramming, and SASP.

F3 signaling primes radiation-induced changes both in GBM and the TME.

To probe the roles of F3 in GBM radiation responses *in vivo*, we performed immunohistochemical staining analyses using human PDX, GBM slice, and syngeneic mouse glioma models (Figure 3). Orthotopic PDX tumor-bearing mice were irradiated, and the brain tissues harvested 5 days later. In regions with a robust upregulation of F3, we found that F3 positively correlated with high levels of fibrin, a key effector in the F3-initiated coagulation cascade (Figure 3A). F3-positive GBM cells were also positive for YKL-40 and CD44 (MES-like GBM markers) and fibronectin 1 (FN1, an ECM protein and MES-like GBM marker)^{9,50,51}. Fibrin polymer and FN1 are known to form a mesh-like structure together, referred to as an oncogenic provisional ECM. It provides a scaffold for recruitment of macrophages, activated platelets, neutrophil extracellular traps (NETs), and traps various growth factors and chemokines⁵². Indeed, we found significant increases in the numbers of TAMs and M2-like TAMs (CD163⁺) in F3-positive, fibrin/FN1 complex-rich regions in the irradiated tumors (Figures 3B, 3C, and S3A).

Human GBM slices resected from newly diagnosed GBM patients maintain *in vivo* tumor architecture and TME including immune cells, endothelial cells, and astrocytes; thus, they can mimic acute responses of human GBM *in situ*²⁴. We prepared acute GBM slices within 6 hours post-surgery, irradiated them *ex vivo*, and then processed for immunostaining and cytokine array analysis 3 days later (Figure S3B). Fibrinogen (precursor of fibrin) and F7 were detected in these GBM slices. Irradiation resulted in robust induction of fibrin/FN1 complexes and CD163⁺ macrophages. Cytokine analysis utilizing 4 sets of matched naïve and irradiated GBM tissue slices consistently showed higher levels of secreted proteins in the conditioned media from irradiated GBM slices (Figure S3C). These data suggest a causal relationship between that RT and fibrin polymerization, an enhanced secretory phenotype, and TAM polarization.

To validate the above findings in the intact immune microenvironment, we employed a *PDGF β* -driven, *p53*-null, syngeneic mouse glioma, a representative proneural subtype tumor⁵³. Naïve tumors showed relatively low basal levels of fibrin, TAMs and CD44⁺ cells. Upon irradiation, however, we found massive increases in fibrin polymerization and TAM infiltration, as well as in levels of F3 and CD44 (Figure 3 D to F). Notably, most of the

CD163⁺, CD206⁺ M2-like TAMs were detected in the fibrin polymer-enriched, F3⁺, CD44⁺ tumor regions, indicating a strong positive correlation between them (Figure 3G). Together, these data further suggest a link between RT-induced coagulation, oncogenic TAMs, and GBM mesenchymal transition.

Molecular mechanisms of F3 signaling in GBM reprogramming and radio-resistance

Given strong spatiotemporal associations between F3 and RT-induced GBM remodeling (Figure 3), we first determined the roles of F3 *in vivo* via shRNA-mediated *F3* knockdown. Non-targeting shRNA or *F3* knockdown (KD) shRNA-expressing GBM cells were transplanted into the brains of nude mice and *in vivo* radiation was started 20 days later (Figure 4 A and B). Immunostaining analysis of the tumor-bearing brain sections revealed that *F3* suppression significantly abrogated RT-induced fibrin polymers and accumulation of IBA1⁺ and CD44⁺ cells (Figure 4A). *F3* knockdown or irradiation alone extended the survival of tumor-bearing mice compared to the control group. Notably, the group injected with *F3* KD cells and given radiation showed far longer survival than all other groups ($p < 0.001$ by log-rank analysis) (Figure 4B).

We then determined the effects of *F3* knockdown on the activation status of NFκB, STAT3, and integrin signaling (Figures 4 and S4). In the naïve state, *F3* knockdown did not induce significant decreases in pp65 and pSTAT3, possibly reflecting low levels of F3. In contrast, *F3* knockdown potently impeded RT-induced upregulation of NFκB, STAT3, and integrin activities, as well as mesenchymal traits (YKL-40 and FN1) (Figures 4 C and D, S4 A and B). Conversely, over-expression of constitutively active mutants of NFκB or STAT3 signaling rescued cell survival of RT-*F3* KD cells, indicating that both NFκB and STAT3 activities are key downstream effectors of RT-induced F3 signaling (Figure 4E).

As RT-F3⁺ GBM cells secrete high levels of SASP factors (Figure 2M) and NFκB activity is a major regulator of SASP factor secretion, we determined the levels of cytokines/chemokines secreted by *F3* KD GBM cells with or without irradiation. RT-induced upregulation of multiple cytokine/chemokines was significantly reduced by *F3* knockdown (Figures 4F and S4C). To investigate the roles of F3 in chemokine-mediated TAM recruitment, we adapted *in vitro* transwell assays using U937 macrophage-like cells (primed U937)⁵⁴. Conditioned media from irradiated GBM cells attracted significantly larger numbers of U937 cells compared to conditioned media from matched naïve cells. *F3* knockdown reduced the levels of macrophage recruitment by ~80% (Figure 4G). Forced activation of NFκB activity but not STAT3 rescued SASP factor secretion in irradiated *F3* knockdown cells and *NFκB* suppression by *p65* shRNA significantly inhibited RT-induced SASP factor secretion, suggesting that RT-induced SASP in GBM is largely dependent on NFκB signaling (Figure 4 H and I).

Conversely, over-expression of F3 in naïve GBM cells showed elevated levels of active NFκB, STAT3 and integrin signaling (Figure S4D). Consistent with this, F3 over-expressing cells were more proliferative in the culture media without the added growth factors and these cells had the enhanced SASP factor secretion compared to the control (Figure S4 E and F). Lastly, the roles of F3 in RT responses in tumor and TME *in vivo* were further confirmed in a doxycycline-mediated inducible *F3* KD system (Figure 4J). These data support that F3 is a

critical regulator for the survival and cell state transition of irradiated GBM cells, as well as for SASP factor secretion.

Recombinant FVII protein impeded radiation-induced coagulation, SASP factor secretion, and TAM accumulation *in vivo*.

The above data collectively suggest that F3 signaling is a critical regulator for post-RT tumor growth and drives an oncogenic TME, making it a potential therapeutic target. Since F3 protein, after binding to its ligand F7, is eventually degraded via the ubiquitin pathway, we hypothesized that specific F7 derivatives may directly trigger F3 degradation without eliciting F3-mediated oncogenic effects⁵⁵. To test, we over-expressed a series of F7 deletion mutants in GBM cells via lentiviral transduction and determined the proliferation of these GBM cells after irradiation (Figure 5A). Through this screen, we found a deletion mutant that potently impeded the growth of irradiated GBM cells, which we designated as FVII (141-amino acid protein without the F7 protease domain).

FVII recombinant protein lacked the pro-coagulation activity unlike wild-type F7 or FVIIa, as determined by *in vitro* coagulation assays (Figure S5A). Instead, FVII robustly induced ubiquitin-mediated degradation of F3 proteins and significantly reduced the level of F3 proteins in irradiated GBM cells (Figure 5 B and C). Consistent with this, irradiated GBM cells treated with FVII for a day showed a significant decrease in phosphorylated p65 and STAT3 proteins (Figure 5D). Furthermore, we found that FVII decreased the levels of the co-immunoprecipitated F3-integrin complexes, HUTS4 (specific for active integrin β 1), and phosphorylated FAK (an immediate downstream effector of integrin signaling) (Figures 5E and S5B). We then determined the effects of FVII on survival and clonogenic growth of GBM cells (Figures 5 F and G). FVII treatment effectively impaired survival of irradiated GBM cells with an IC₅₀ in the 0.1 to 1 nM range (Figure 5F). In contrast, normal neural progenitor cells (NPCs) and primary astrocytes did not exhibit cytotoxicity even at micromolar FVII concentration (Figure 5F). Unlike GBM cells, normal brain cells showed little change in the levels of pFAK and pERK after FVII treatment, partially explaining GBM-specific cytotoxicity of FVII (Figure S5C). Real-time cell imaging analysis demonstrated that FVII treatment potently impaired clonogenic growth of irradiated F3^{high} GBM cells (Figure 5G). GBM cells treated with FVII showed disruption of mitochondrial membrane potential and defective mitochondrial structure (Figure S5 D to F). Lastly, to determine the effects of FVII on SASP factor secretion, we treated irradiated GBM cells with FVII for 1 day and collected the conditioned culture media. FVII treatment significantly diminished the secretion of cytokines (Figure 5H). Together, these data suggest that FVII is a potent anti-GBM agent that mitigates F3-mediated oncogenic signaling, especially in combination with RT.

To determine *in vivo* effects of FVII, we started with subcutaneous tumor models. We irradiated human PDX tumors focally when the tumors reached ~500 mm³ and administered FVII protein (50 μ g/kg body weight) via intravenous injection. Compared to the naïve controls, tumors harvested 5 days after radiation showed marked increases in fibrin/FN1 complexes, tumor-infiltrating CD11b⁺, F4/80⁺, CCR2⁺ immune cells and CD163⁺ M2-like TAMs, along with massive upregulation of F3 (Figure 5I and data not shown). Notably,

FVII treatment potently inhibited all the above changes, with a dramatic increase in the number of cleaved-caspase 3 (C-Cas3)⁺ cells (Figure 5I). To evaluate *in vivo* effects of FVII on signaling pathway activation and senescence-like characteristics, we harvested the tumors from each group and processed for further analyses. FVII treatment significantly reduced RT-induced cell survival signaling such STAT3, but increased levels of cell death-associated proteins in tumor (Figure 5J). RT-induced SA-βGal⁺ reactivities were significantly decreased by FVII treatment and clonogenic capacities of sorted RT-C₁₂FDG⁺ cells isolated from these tumors were significantly abolished by *in vivo* FVII treatment (Figure S5 G and H). To analyze the chemokine/cytokine microenvironment within the tumors treated with radiation, FVII, or both agents, we performed cytokine profiling assays using tumor lysates. Irradiation induced significant upregulation of secreted proteins, many of which have well-known functions for macrophage recruitment, M2-like TAM polarization, and cell state transition. Notably, FVII treatment significantly and globally repressed the chemokine/cytokine levels (Figures 5K and S5I).

To determine the effects of tumors and FVII on systemic hemostasis, we measured the blood clotting activities by standard tail bleeding assays (Figure 5M). Compared to the control mice, tumor-bearing mice had shorter blood clotting time, which was further shortened by irradiation. While FVII treatment on non-tumor bearing mice did not affect blood clotting time, the combination of irradiation and FVII reverted hypercoagulation state in the RT-tumor bearing mice to near-normal range (Figure 5M). Studies of tumor growth kinetics showed that irradiation or FVII monotherapy alone suppressed tumor growth rate to about 50 to 60 % of that of naive tumors, but the effect of either agent alone was transient and led to rapid regrowth (Figure 5L and 5N). In contrast, combination therapy yielded near-complete tumor regression (Figure 5N).

FVII therapies radio-sensitize GBM tumors in orthotopic PDX models.

We tested the effects of FVII recombinant protein in orthotopic GBM PDX models using patient-derived 022 or 827 GBM cells. Irradiation was started 20 days (for 827 tumor) or 25 days (for 022 tumor) after tumor cell implantation and FVII protein was delivered via intravenous injection, concurrently with irradiation (Figures 6A and S6A). Five days after irradiation, the brains from each group were harvested for immunostaining (n=3) and immunoblot analysis through tumor dissection (n=3). Combination treatment with irradiation and FVII greatly diminished RT-induced fibrin accumulation, MES cell state transition, TAM polarization, and activities of integrin and NFκB signaling, but increased numbers of C-cas3⁺ cells (Figure 6 A to D). Notably, histological examination of the brain sections from the mice receiving combined treatment at 38 days after implantation (the time when RT-treated mice were sacrificed) showed few tumor cells and only faint staining for fibrin polymers (Figure 6E). We also determined the effects of orthotopic GBM tumors and FVII on systemic hemostasis by D-dimer and tail bleeding assays (Figure 6 F and G). Similar to subcutaneous tumor results (Figure 5M), FVII treatment potently inhibited the hypercoagulatory state in RT-tumor bearing mice (Figure 6 F and G). Lastly, irradiation or FVII monotherapy alone extended survival of tumor-bearing mice by about 10 days compared to the control group (Figure 6H). Notably, the group that received combination

therapy showed a far greater survival extension, with about 50 % of mice surviving and lacking detectable tumors three months later (Figure 6H).

While several studies have reported that the blood-brain barrier (BBB) is functionally disrupted in some GBM⁵⁶, the highly infiltrative GBM cells in the neighboring brain parenchyma presents technical challenges in developing effective anti-GBM therapeutics. As an independent but complementary therapeutic approach to FVII recombinant protein, we developed a neural progenitor cell (NPC)-based cellular vector system. NPCs have intrinsic tumor-homing properties and survive well in the brains^{57,58}. Lentivirally transduced FVII-expressing NPCs were viable and maintained stable levels of secreted FVII (Figure S6B). Upon co-culture with irradiated GBM cells, FVII-expressing NPCs but not the control NPCs induced massive GBM cell death (Figure S6B). To mimic a clinical scenario in newly diagnosed human glioma patients, we injected FVII-expressing NPCs into the established PDX tumors, followed by head-only irradiation two days later (Figure S6 C and D). Similar to the RT and FVII combination, co-treatment with RT and FVII-NPCs greatly diminished RT-induced F3 induction and activities of pro-tumorigenic signaling, leading to longer survival of tumor-bearing mice (Figures S6 C to E).

Recurrent tumors from early-relapse GBM patients harbor the upregulated gene signatures for the senescence and coagulation pathways.

Comparison of matching primary and recurrent GBMs can inform therapy-induced phenotypic tumor evolution, including GBM cell state and associations between TME components. We therefore analyzed transcriptional profiles of primary GBMs (n = 25) treated with radiation therapy and separated early relapses (Progression-free survival (PFS) < 6 months, n = 11) from late relapses (PFS >12 months, n = 14) using the dataset from GLASS consortium (Figure 7)^{50,59}. The status of pathway activation in each tumor was inferred by the pathway enrichment scores from representative gene signature sets^{9,14,60,61} (Figure 7 A and B). We observed no significant differences in signature gene set levels between primary tumors with early and late relapse. When comparing relapsed GBMs, however, we found that early-relapse GBMs showed a significantly higher predicted presence of M2 macrophages and the enrichment of senescence, coagulation, and NFκB signatures compared with late-relapse GBMs⁵⁰ (Figure 7B). Furthermore, the enrichment scores for senescence, coagulation, and NFκB signatures highly correlated with each other, especially in the early-relapse tumor pairs (Figure 7 C and D). These data are consistent with our findings and may provide clinical relevance for potential translation of FVII-based therapies.

We then determined whether F3 targeting can be combined with other anti-cancer therapeutic approaches. A combination therapy with TMZ and FVII, and triple combination of RT, TMZ, and FVII significantly prolonged the survival of tumor-bearing mice (Figure S7A). Aberrant activation of the EGFR, MET, and AKT pathways is frequently found in GBM, and each pathway has been established as a potential therapeutic target^{62,63}. We treated 4 different GBM cells with representative EGFR, MET, and AKT inhibitors and FVII (Figure S7B). Combination treatment robustly induced tumor cell death and impaired the clonogenic growth of GBM cells to a much greater degree than monotherapy alone

(Figure S7C). Lastly, pre-metastatic MG63 osteosarcoma model revealed RT-induced F3 signaling very similar to GBMs, raising the possibility that our findings on RT-induced F3 signaling may be applicable to other cancer types (Figure S7 D to H).

Our data collectively support the previously unidentified concept that activation of F3 signaling during therapy-induced senescence is a central initiator to trigger global adaptation programs in tumor cells and in the TME, leading to therapy resistance and tumor recurrence (Figure 7E).

Discussion

We show that radiation-induced SA- β Gal⁺ GBM cells robustly contribute to post-RT tumor regrowth by active clonal expansion and global reorganization of immune, ECM, and cytokine landscapes in the TME. F3 proteins are rapidly elevated in the SA- β Gal⁺ GBM cells upon irradiation, and F3 signaling promotes clonal expansion, mesenchymal-like cellular state transition, and secretion of oncogenic SASP factors and ECM proteins. Concurrently, F3 also initiates a hyperactive coagulation cascade including local fibrin polymers, which in turn facilitates TAM accumulation/polarization and ECM remodeling in the tumor regions. These F3-initiated cellular events are functionally linked, and together they constitute an oncogenic feed-forward loop, in which TAMs and SASP factors are critical players. In fact, F3 appears to be a master switch regulating the radiation response in GBM, with striking effects on senescence-like and mesenchymal tumor phenotypes as well as the microenvironment. We also demonstrate a strategy to inhibit oncogenic F3 signaling as an anti-GBM therapeutic approach. These data collectively support that F3 is a critical driver of oncogenic senescence and therapeutic resistance in GBM, opening potential therapeutic avenues for F3 targeting.

We report here the existence of an F3-driven phenotype in GBM sharing some features of senescent cells—including SA- β Gal reactivity, senescence marker expression (HP1J and H3K9me3), enrichment of representative senescence gene sets, and SASP-like secretory phenotype—with features of GBM stem cells. On the other hand, robust clonal expansion of irradiated SA- β Gal⁺ GBM cells is different from traditional view of cellular senescence in which irreversible cell cycle arrest is a central tenet. Our findings are highly consistent with recent studies showing that the senescence program activates key stemness signaling pathways such as WNT and YAP^{44,64} and that the senescent state in cancer is highly dynamic and reversible⁴⁴. Thus, we propose the cellular states of irradiated SA- β Gal⁺ GBM cells as the senescence-like GBM cell phenotype without stable cell cycle arrest.

At the early stages of tumor initiation, oncogene-induced senescence (OIS) is an essential tumor-suppressive barrier that limits expansion of pre-malignant cells. It has been generally thought that cells under OIS remain arrested due to activation of TP53 and/or Cdkn2a pathways, however, a subset of these cells escapes from OIS and progresses to more aggressive stages⁶⁵. GBM harbors defects in apoptosis and cell cycle regulators such as homozygous deletion of *Cdkn2a* and deregulated TP53 pathways, possibly enabling bypass of cell cycle arrest while adopting other pro-tumorigenic features of senescence. It is increasingly clear now that various therapies including irradiation, chemotherapeutics,

and targeted inhibitors induce massive numbers of senescent or senescent-like cells in malignant cancers^{15,66}. In most of these studies, however, senescent-like tumor cells have been identified by colorimetric SA- β Gal assay and very limited senescent cell marker staining without cell fate determination. Our findings in GBM may provide a clue to better characterize TIS in other malignancies.

The close relationship between cancer and thrombosis has been recognized by Trousseau since 1865⁶⁷. Hyper-coagulability can lead to serious, life-threatening conditions such as venous thromboembolism (VTE). VTE is frequently found in cancer patients, among whom high-grade glioma patients showed the highest incidence^{52,68}. F3, originally identified as an initiator of a stress-responsive coagulation cascade, has been implicated in hyper-coagulation activities in cancer, pro-proliferative signaling, and tumor dormancy, and metastasis^{38,40,52,69,70}. A more recent study reported that F3 is preferentially expressed in quiescent stem-like GBM cells⁴². In addition, increased blood clotting activities and aberrant fibrin clots have frequently been observed in patients with senescence-associated pathologies including COVID, tissue injury, and aging⁷¹⁻⁷⁴. Our findings may suggest the possibility that senescence plays a causal role in hypercoagulation activity in non-cancer pathologies as well.

Various therapeutic approaches that target senescent tumor cells and/or senescence-associated pathways have been developed as potential anticancer approaches⁶⁶. These approaches can be largely classified into three categories: (i) targeting individual oncogenic SASP factors^{75,76}, (ii) targeting individual stemness/survival pathways that are particularly induced by the TIS program^{44,77}, and (iii) targeting senescent tumor cells with senolytic approaches⁷⁸. Similar to the highly overlapping RTK signaling networks found in cancer, post-therapy malignant tumors secrete multiple SASP factors with very similar or redundant functions^{11,75,79-83}. TIS-associated epigenetic reprogramming may reactivate multiple, potentially redundant, oncogenic transcription networks^{44,64,77}. Our data suggest that FVII targeting approach can be developed into a viable therapeutic option. F3 targeting potentially inhibited radiation-induced TAM accumulation and oncogenic TAM polarization, indicating a potential intersection with TAM re-education approaches and/or other immune-based anti-cancer approaches. We postulate that F3 signaling is a crucial hub triggering multiple oncogenic pathways in the therapy-induced tumor cell senescence setting.

As senescence in the brain parenchyma and immune landscapes are likely critical for RT-induced remodeling and GBM radio-resistance, extensive studies in syngeneic tumor models can provide deeper understanding of associations between immune, microenvironmental components and treatment response. Most of our data were obtained from PDX-bearing immunocompromised mice models. Despite this caveat, our data reveal that F3 signaling in GBM is an active adaptation program to evade therapeutic pressure and leverage oncogenic aspects of therapy-induced senescence. Thus, inhibiting F3 signaling may represent a promising strategy to markedly enhance otherwise suboptimal anti-GBM therapies. Our findings may provide a step forward to a better understanding of F3 signaling, which may be critical for advancing therapeutic strategies.

STAR METHODS TEXT

RESOURCE AVAILABILITY

Lead contact—Further information and requests for resources and reagents should be directed to and will be fulfilled by the lead contact, Jeongwu Lee (leej7@ccf.org).

Materials availability—Materials generated in this study are available from the lead contact upon request.

Data and code availability—The datasets generated during this study are available at GEO under accession number GEO; GSE162931. Any additional information required to reanalyze the data reported in this paper is available from the lead contact upon request.

METHOD DETAILS

Patient-derived glioblastoma specimens and derivatives—Following written informed consent, tumor samples classified as GBM, based on the WHO criteria, were obtained from patients undergoing surgical treatment in accordance with the NIH, Cleveland Clinic Lerner Research Institute, and Samsung Medical Center Institutional Review Boards. Within 1 to 6 hours after surgical removal, tumors were washed in PBS and processed for the following models.

GBM spheroids: Tumor cells were cultured in Neurobasal medium supplemented with N2, B27 and bFGF and EGF (NBE medium; Neurobasal media, N2 and B27 supplements (0.5x each; Invitrogen), and human recombinant bFGF and EGF (25 ng/mL each; R&D Systems)^{47,84}.

GBM organoids: GBM organoids display tumor cell hierarchy and differentiation heterogeneity by oxygen/nutrient gradient. Tissue pieces were cut into 0.5 to 1 mm diameter and cultured in the dishes on top of an orbital shaker rotating at 120 rpm at 37°C in a 5% CO₂, 95% humidity incubator^{22,23,85}.

GBM slices: GBM tissue pieces were sliced using a vibrating blade microtome into 3 to 5 mm diameter, 300 μm thick slices and transferred to a culture dish.

Primary cell cultures—Normal NPCs derived from human embryonic stem cells (H9, Invitrogen, Cat # N7800100) and aborted fetal brain tissues (Lonza, Cat # PT-2599) were cultured in NBE media or neural progenitor maintenance media (Lonza, Cat# CC-3209). Primary human astrocytes (Lonza, Cat# CC-2565) were cultured in astrocyte growth media (Lonza, Cat# CC-3186). Human U937 cells from ATCC (CRL-1593.2) were maintained in RPMI 1640 media (Gibco, 11875093) with 10% FBS (Gibco, 10438026), and 1 % penicillin/streptomycin (Gibco, 15140148). For all co-culture experiments, FBS serum was not used.

Patient-derived xenograft (PDX) and RCAS-TVA mouse glioma models—All mice experiments were performed according with the IACUC approved protocols. For orthotopic tumor implantation, GBM cells were injected intracranially into the striatum of nude mice (BALB/c nu/nu) by using a stereotactic device (Kopf instruments, coordinates:

2 mm anterior, 2 mm lateral from the bregma, 2.5 mm depth from the dura) as previously described⁴⁷. For *F3* inducible knockdown, drinking water containing doxycycline (D9891, Sigma, 2mg/ml) and 5% sucrose was given at 20 days after injection. The water was protected from light and exchanged every 2 days. Syngeneic RCAS-TVA mouse gliomas induced by *PDGFB* overexpression in *p53*-null background were generated as previously reported⁵³. When mice develop neurological symptoms (lethargy, ataxia, and seizures) or significant body weight loss, mice were killed and processed for histological analysis.

Lung metastasis model—Naïve or irradiated MG63 cells (5×10^5) were injected into the tail vein of each nude mice (BALB/c nu/nu).

FVII-mediated therapy in animal models—All mice were randomly assigned to appropriate treatment groups. For recombinant FVII protein experiments, FVII proteins (50 µg/kg body weight) were administered via intravenous injection daily, concurrent with irradiation or temozolomide treatment (25 mg/kg body weight, intraperitoneal injection, T2577, Sigma)⁸⁶. For FVII-expressing NPC experiments, NPCs (1×10^6 cells per mice) were injected into the brains of tumor-bearing mice, two days before irradiation.

Blood clotting time test—To determine tail-bleeding time, mice were kept under anesthesia and placed on a heating pad. Distal tail was cut at 5 mm from the tip and immediately submerged into 10 ml PBS at 37 °C⁸⁷.

D-dimer ELISA assays—Plasma was collected in 3.2% buffered sodium citrate tube from each sample for D-dimer detection. The amount of D-dimer was assayed using mouse D-dimer ELISA kit (Novus Biologicals, NBP3-08100) according to manufacturer's protocol.

Radiation regime—For irradiation of tissues and cells, a single dose of 3Gy, 5Gy, or 10 Gy was used. For *in vivo* irradiation, the anesthetized mice were placed in a lead shielding device in which the brains or subcutaneous tumors were exposed. Localized radiation was performed with either a single dose of 10 Gy or a fractionated regime (2Gy daily for 5 days).

Senescence-Associated β -Galactosidase (SA- β Gal) reactivity assays—For colorimetric SA- β Gal assay, we used senescence- β -galactosidase kit (9860, Cell Signaling). Briefly, samples were incubated with β -galactosidase staining solution (pH 6.0) at 37°C in a dry incubator without the added CO₂. Staining images were analyzed using an inverted fluorescence microscope (DM4000 B, Leica). For fluorometric SA- β Gal staining assay, live cells or tissues were pre-treated with bafilomycin A1 (B1793, Sigma-Aldrich, 100 nM) and then cultured with C₁₂FDG (5-Dodecanoylamino fluorescein Di- β -D-Galactopyranoside, D2893, Invitrogen) as described with minor modifications²¹. C₁₂FDG intensity was analyzed by LSR II Fortessa flow cytometer (BD) or confocal microscope.

Fluorescence activated cell sorting (FACS)—Cell sorting was performed using BD FACS Aria II. GBM cells were stained with either C₁₂FDG or F3 antibody (BD 550312 1:20), and each subpopulation was sorted based on the levels of staining intensities. A matched isotype antibody was used as a control and propidium iodide (PI, 5 µg/ml) was used for live/dead cell determination. To ensure purity and viability of the sorted subpopulations,

we repeated flow cytometry analysis and PI staining after initial sorting. Data were collected and analyzed using FlowJo software.

Flow cytometry analysis—Dissociated GBM cells were incubated with 5% donkey or goat serum, 2mM EDTA in PBS for 30 minutes to block non-specific binding, and then labeled with anti-F3-FITC antibody (BD 550312, 1:20), Nestin (SC-23927, 1:100), H3K9me3 (ab8898, 1:100), or ABCG2 (BD562167, 1:100) in 5% serum containing PBS for 1 hour. For detection of intracellular proteins, cells were permeabilized with 0.1% saponin (S7900, Sigma-Aldrich). After gently wash by cold PBS, the cells then incubated with Alexa Flour secondary antibodies (Invitrogen, 1:400) for additional 30 minutes.

Annexin V staining and mitochondria TMRE assays were performed using standard detection kits (ab113852, Abcam). Flow cytometry assays were performed using at least three independent biological samples.

***In vivo* clonal analysis using barcode-sequencing**—GBM cells were transduced with Clone Tracker 50M lentiviral barcode library (BC13X13V, Collecta Inc.). For *in vivo* clonal analysis, transduced GBM cells were injected into the brains of nude mice. Genomic DNA was extracted from the resultant tumor tissues using QIAamp DNeasy Blood and Tissue kit (69504, Qiagen) following manufacturer instructions. Barcodes from the tumor were amplified using sample-specific primer sets provided in the NGS prep kit (LNGS-200, Collecta Inc.). Library quality and fragment sizes were assessed on a Fragment Analyzer before high-throughput sequencing on a HiSeq. Sequence processing and analysis were performed by using Collecta NGS Demultiplexing and Alignment software.

Cell surface marker screening—BD lyoplate human cell surface marker screening panel contains 242 purified monoclonal antibodies against human clusters of differentiation (CD) markers (560747, BD). Patient-derived GBM cells (131 and 559) were used for cell surface marker screening. Briefly, GBM cells (about 1.5×10^8) were dissociated with Accutase (A6964, Sigma-Aldrich) and incubated with bafilomycin A1 (100 nM) and C₁₂FDG (33 μ M) for 2 hours at 37°C or anti-F3-FITC for 1 hour at 4°C. After C₁₂FDG or F3 staining, cells were split and incubated with each CD antibody for 1 hour at 4°C. Flow cytometry data were measured using LSRII HTS system and analyzed using FlowJo software (NIH).

Single cell RNA-sequencing (scRNA-seq) and bulk RNA-seq analysis—Cells were dissociated with Accutase and suspended in 1% BSA PBS solution. Live cell FACS sorting was performed with DRAQ5 fluorescent probe (62251, Thermo Fisher Scientific). Cell vitality was determined by trypan blue staining and live cells were diluted to a final concentration of 1000 viable cells/ μ L in 0.1% BSA PBS solution. Each sample had over 90% viability. ScRNA-seq library preparation and sequencing were performed as previously reported^{23,26}. Briefly, scRNA-seq data were processed through 10x Genomics Chromium Single Cell Platform, and count matrices were generated using their Cell Ranger pipeline (10x Genomics). ScRNA-seq data were analyzed using scanpy. For quality control, genes detected in less than 5 cells and cells with fewer than 1000 genes were excluded. Expression values were corrected to 100,000 reads per cell and transformed. Unbiased

clustering was performed by UMAP dimensionality reduction visualization analysis²⁶. Gene signature sets used in this report are; GBM subtype⁸⁸, stemness^{25,42}, cell cycling²⁶, NFκB⁹, senescence^{60,61,89}, and coagulation¹⁴.

ATAC-sequencing analysis—Cells were stained with either C₁₂FDG or F3 antibody (BD 550312, 1:20), and each subpopulation was sorted using BD FACS Aria II. Propidium iodide (PI, 5 μg/ml) was used for live/dead cell determination. 5 × 10⁵ cells / sample were used for ATAC-Seq Library Preparation (K1157, APExBio). Briefly, cells were resuspended in 50μl ATAC lysis buffer containing (0.5 μl 10% NP40, 0.5 μl 10% Tween 20, and 0.5 μl 2% Digitonin) for 3 min on ice and then cold ATAC lysis buffer containing (0.5 μl 10% Tween 20) was added. Nuclei were centrifuged at 1000 rpm for 10 min at 4°C in a fixed angle. Nuclei were resuspended in 50μl tagmentation master mix containing (5μl transposase, 16.5μl PBS, 0.5μl 2% Digitonin, 0.5 μl 10% Tween 20, 2.5μl water, and 25μl 2x tagmentation buffer). The tagmentation reaction was incubated at 37°C for 30 min in a thermomixer with 1000 rpm. Reactions were cleaned up with DNA purification kit (28104, Qiagen). Libraries were amplified and sequenced on a Nextseq instrument (Illumina).

Bioinformatics data analysis—Analysis for genomic alterations including amplification, deletion, and mutation of key genes and glioma subtype assignment were performed, as described^{50,59,62,88,90}. Pearson correlation coefficient was calculated by “cor” function of R and Pearson’s Chi-squared Test was conducted using “chisq.test” function of R with default settings.

Chemokine/Cytokine profiling assays—Conditioned media was filtered through 0.2 μm filters (Sartorius Stedium Biotech). Filtered media or cell lysates were incubated with Human Cytokine antibody array kit (AAH-CYT-1000, RayBiotech). Intensity of each spot was measured using ImageJ and analyzed using the RayBiotech analysis tool (AAH-ANG-1000, RayBiotech). Heatmaps were generated by “heatmap.2” function of R package.

Lentivirus—Human HEK293 cells (ATCC) were cultured in DMEM media supplemented with 10% FBS, 1% penicillin and streptomycin. For viral production, 293T cells were co-transfected with the corresponding lentiviral vector and packaging plasmids (psPAX2 and pCMV-VSV-G) using CalPhos Mammalian Transfection Kit (631312, Clontech). Virus-containing supernatants were collected and concentrated by Lenti-X concentrator (631231, Clontech).

All expression vectors were cloned into pLenti6/V5 vector (K495500, Invitrogen) and validated by sequencing and immunoblot analysis. Expression vectors used in this study include wildtype *F3*, wildtype *F7*, *F7* deletion series, STAT3C mutant, and *IKK-2 S177E S181E (IKK2SSEE)* mutant (a gift from Anjana Rao, Addgene plasmid # 11105)⁹¹. A series of *F7* deletion mutants was designed to include and/or exclude domains of *F7* proteins. Short hairpin RNA (shRNA)-expressing lentiviral vectors were purchased from Sigma-Aldrich and doxycycline-inducible shRNA plasmids were purchased from Dharmacon. *F3* or *pp65* shRNA constructs were tested and at least two independent shRNA knockdown vectors were selected for further studies.

FVII recombinant proteins—We designed various recombinant variant FVII proteins including FVII and S404A FVII mutant as well as wild type FVII⁹². Recombinant FVII variant proteins including wildtype F7, S404A F7, and FVII (181 amino acid protein without peptidase S1 domain; 141 amino acid protein in a secreted form) were synthesized (Genscript) and validated by immunoblot analysis, *in vitro* clotting assay (factor 7 human chromogenic activity Assay; ab108830, Abcam), and cysteine bond determination by MASS spectrometry.

Immunofluorescence analysis—Tissue slices were harvested 1 to 3 days after irradiation and fixed in 4% PFA (SC281692, Santa Cruz biotechnology). To prepare the frozen sections of tumors, samples were washed in PBS, cryoprotected in 30% sucrose (S0389, Sigma-Aldrich) at 4°C overnight, embedded in O.C.T compound (4583, SAKURA Tissue Tek), and sectioned using a cryostat (CM3050S, Leica). Tissue sections and cells were blocked using a blocking solution (0.3% Triton X-100, 5% goat or donkey serum, 1% BSA in PBS) for 1 hour at room temperature. For mouse tissue sections, mouse-on-mouse blocking reagent (MKB-2213, Vector Laboratories) was added to the blocking solution. Immunofluorescence images were taken using a Leica TCS SP5 Confocal Microscope.

Immunohistochemistry analysis (IHC)—Paraffin sections were prepared in the Cleveland Clinic Lerner Research Institute imaging core. For immunohistochemistry analysis (IHC), tissue sections were deparaffinized in xylene (214736, Sigma-Aldrich) and rehydrated through ethanol gradient. Antigen retrieval was achieved by microwaving the sections in Unmasking solution (citrate based buffer, pH 6.0, H-3300, Vector Laboratories). Endogenous peroxidase activity was blocked by incubation with BLOXALL blocking solution (SP-6000, Vector Laboratories). All images were taken by slide scanner Leica SCN400 microscope and analyzed by Imagescope and ImageJ.

Immunoblots and co-immunoprecipitation—Cells were lysed in Pierce IP lysis buffer (25 mM Tris-HCl pH 7.4, 150 mM NaCl, 1 mM EDTA, 1% NP-40, and 5% glycerol; #87788, Thermo) supplemented with protease inhibitors cocktail (Complete Mini, 11836153001, Sigma-Aldrich) and phosphatase inhibitor (#78428, Thermo), incubated on ice for 30 minutes and cleared by centrifugation at 4°C for 20 minutes. For immunoprecipitation, protein lysates were incubated with appropriate antibodies for overnight at 4 °C. Protein bands were visualized using ECL Western Blotting Detection Reagents (RPN2232, GE Healthcare) and subjected to densitometry analysis using ImageJ.

Cell growth, viability, drug treatment, and soft agar colony forming assays—Standard methods including cell counting and MTT assays (11465007001, Sigma-Aldrich) were used. Cilengitide (1 to 5 μM, S6387, Selleckchem), integrin blocking antibody (ab24693, Abcam), and cucurbitacin (100 nM, C4493, Sigma-Aldrich) were used to inhibit integrin or STAT3 signaling, respectively.

Soft agar colony forming assays were performed to determine capacity of clonogenic cell growth by counting single cell-driven colonies. GBM cells were mixed with top agar (Neurobasal media, N2 and B27, 0.4% agarose) and layered on top of 0.8% agarose.

Medium with fresh FVII (100 ng/ml) was added every 3 days. Three weeks later, colonies were fixed with 4% PFA and stained with 0.5% crystal violet.

Macrophage recruitment assay—Immune cell recruitment capacity of GBM cells and U937 cells was measured using transwell inserts (8 μ m pore size, 3422). The cells were subsequently fixed with 4% paraformaldehyde at room temperature for 15 min and stained with crystal violet at room temperature for 10 min.

NF κ B, STAT3, and TCF/LEF reporter assays—To determine transcriptional activities of the above pathways, cells were transduced with lentiviral constructs containing NF κ B consensus element, STAT3 binding elements, and TCF/LEF transcriptional response elements with the minimal promoter red firefly luciferase reporter gene (Systems Biosciences). Luciferase intensities were measured by ONE-Glo Luciferase Assay System according to manufacturer's protocol (E6110, Promega).

Transmission electron microscopy (TEM)—Cells were fixed in 2.5% glutaraldehyde / 4% PFA in 0.1M sodium cacodylate buffer at 4°C overnight. Cell suspension samples were washed and treated with 1% osmium tetroxide for 1 hour, stained with 1% uranyl acetate, dehydrated, and then embedded in LX-112. Samples were analyzed using Zeiss EM 10 transmission electron microscope.

Real-time live cell imaging analysis—Cell growth was monitored by using Incucyte live cell analysis system (Essen Bioscience). Confluency of each well was determined every 3 hours for the entire experimental periods.

Quantitation and statistical analysis

All data were expressed as means \pm SD from at least three independent experiments. Quantification of immuno-positive cells in immunostaining analyses was carried out using NIH imageJ software (National Institutes of Health, Bethesda, MD). For the animal survival studies, p values were determined by log-rank test. Student's t-test or ANOVA were used to determine statistical significance. Pearson correlation coefficient was calculated by "cor" function of R.

Supplementary Material

Refer to Web version on PubMed Central for supplementary material.

ACKNOWLEDGEMENTS

This work was supported by NIH grants R01 NS082312, R01 CA223770 and Velosano cancer grant (to J.L).

INCLUSION AND DIVERSITY

All authors of this paper support inclusive, diverse, and equitable conduct of research.

References

1. Gilbert MR, Dignam JJ, Armstrong TS, Wefel JS, Blumenthal DT, Vogelbaum MA, Colman H, Chakravarti A, Pugh S, Won M, et al. (2014). A randomized trial of bevacizumab for newly diagnosed glioblastoma. *N Engl J Med* 370, 699–708. 10.1056/NEJMoa1308573. [PubMed: 24552317]
2. Lim M, Xia Y, Bettgowda C, and Weller M (2018). Current state of immunotherapy for glioblastoma. *Nat Rev Clin Oncol* 15, 422–442. 10.1038/s41571-018-0003-5. [PubMed: 29643471]
3. Stupp R, Mason WP, van den Bent MJ, Weller M, Fisher B, Taphoorn MJ, Belanger K, Brandes AA, Marosi C, Bogdahn U, et al. (2005). Radiotherapy plus concomitant and adjuvant temozolomide for glioblastoma. *N Engl J Med* 352, 987–996. 10.1056/NEJMoa043330. [PubMed: 15758009]
4. Bao S, Wu Q, McLendon RE, Hao Y, Shi Q, Hjelmeland AB, Dewhirst MW, Bigner DD, and Rich JN (2006). Glioma stem cells promote radioresistance by preferential activation of the DNA damage response. *Nature* 444, 756–760. 10.1038/nature05236. [PubMed: 17051156]
5. Chen J, McKay RM, and Parada LF (2012). Malignant glioma: lessons from genomics, mouse models, and stem cells. *Cell* 149, 36–47. 10.1016/j.cell.2012.03.009. [PubMed: 22464322]
6. Barker HE, Paget JT, Khan AA, and Harrington KJ (2015). The tumour microenvironment after radiotherapy: mechanisms of resistance and recurrence. *Nat Rev Cancer* 15, 409–425. 10.1038/nrc3958. [PubMed: 26105538]
7. Yoo KC., Suh Y., An Y., Lee HJ., Jeong YJ., Uddin N., Cui YH., Roh TH., Shim JK., Chang JH., et al. (2018). Proinvasive extracellular matrix remodeling in tumor microenvironment in response to radiation. *Oncogene* 37, 3317–3328. 10.1038/s41388-018-0199-y. [PubMed: 29559744]
8. Winchell HS, Anderson AC, and Pollycove M (1964). Radiation-Induced Hemorrhagic Diathesis in Dogs Unassociated with Thrombocytopenia: Association with an Intravascular Protein-Polysaccharide Particle. *Blood* 23, 186–192. [PubMed: 14122243]
9. Bhat KPL, Balasubramanian V, Vaillant B, Ezhilarasan R, Hummelink K, Hollingsworth F, Wani K, Heathcock L, James JD, Goodman LD, et al. (2013). Mesenchymal differentiation mediated by NF-kappaB promotes radiation resistance in glioblastoma. *Cancer Cell* 24, 331–346. 10.1016/j.ccr.2013.08.001. [PubMed: 23993863]
10. Halliday J, Helmy K, Pattwell SS, Pitter KL, LaPlant Q, Ozawa T, and Holland EC (2014). In vivo radiation response of proneural glioma characterized by protective p53 transcriptional program and proneural-mesenchymal shift. *Proc Natl Acad Sci U S A* 111, 5248–5253. 10.1073/pnas.1321014111. [PubMed: 24706837]
11. Hara T, Chanoch-Myers R, Mathewson ND, Myskiw C, Atta L, Bussema L, Eichhorn SW, Greenwald AC, Kinker GS, Rodman C, et al. (2021). Interactions between cancer cells and immune cells drive transitions to mesenchymal-like states in glioblastoma. *Cancer Cell* 39, 779–792 e711. 10.1016/j.ccell.2021.05.002. [PubMed: 34087162]
12. Ahmed MM, Hodge JW, Guha C, Bernhard EJ, Vikram B, and Coleman CN (2013). Harnessing the potential of radiation-induced immune modulation for cancer therapy. *Cancer Immunol Res* 1, 280–284. 10.1158/2326-6066.CIR-13-0141. [PubMed: 24777964]
13. Kennedy AR, Maity A, and Sanzari JK (2016). A Review of Radiation-Induced Coagulopathy and New Findings to Support Potential Prevention Strategies and Treatments. *Radiat Res* 186, 121–140. 10.1667/RR14406.1. [PubMed: 27459701]
14. Magnus N, Gerges N, Jabado N, and Rak J (2013). Coagulation-related gene expression profile in glioblastoma is defined by molecular disease subtype. *J Thromb Haemost* 11, 1197–1200. 10.1111/jth.12242. [PubMed: 23582031]
15. Ewald JA, Desotelle JA, Wilding G, and Jarrard DF (2010). Therapy-induced senescence in cancer. *J Natl Cancer Inst* 102, 1536–1546. 10.1093/jnci/djq364. [PubMed: 20858887]
16. Schmitt CA, Wang B, and Demaria M (2022). Senescence and cancer - role and therapeutic opportunities. *Nat Rev Clin Oncol* 19, 619–636. 10.1038/s41571-022-00668-4. [PubMed: 36045302]
17. Gorgoulis V, Adams PD, Alimonti A, Bennett DC, Bischof O, Bishop C, Campisi J, Collado M, Evangelou K, Ferbeyre G, et al. (2019). Cellular Senescence: Defining a Path Forward. *Cell* 179, 813–827. 10.1016/j.cell.2019.10.005. [PubMed: 31675495]

18. He S, and Sharpless NE (2017). Senescence in Health and Disease. *Cell* 169, 1000–1011. 10.1016/j.cell.2017.05.015. [PubMed: 28575665]
19. TCGA (2008). Comprehensive genomic characterization defines human glioblastoma genes and core pathways. *Nature* 455, 1061–1068. nature07385 [pii] 10.1038/nature07385. [PubMed: 18772890]
20. Dimri GP, Lee X., Basile G., Acosta M., Scott G., Roskelle C., Medrano EE., Linskens M., Rubelj I, Pereira-Smith O., and et al. . (1995). A biomarker that identifies senescent human cells in culture and in aging skin in vivo. *Proc Natl Acad Sci U S A* 92, 9363–9367. 10.1073/pnas.92.20.9363. [PubMed: 7568133]
21. Debacq-Chainiaux F, Erusalimsky JD, Campisi J, and Toussaint O (2009). Protocols to detect senescence-associated beta-galactosidase (SA-beta-gal) activity, a biomarker of senescent cells in culture and in vivo. *Nat Protoc* 4, 1798–1806. 10.1038/nprot.2009.191. [PubMed: 20010931]
22. Hubert CG, Rivera M, Spangler LC, Wu Q, Mack SC, Prager BC, Couce M, McLendon RE, Sloan AE, and Rich JN (2016). A Three-Dimensional Organoid Culture System Derived from Human Glioblastomas Recapitulates the Hypoxic Gradients and Cancer Stem Cell Heterogeneity of Tumors Found In Vivo. *Cancer Res* 76, 2465–2477. 10.1158/0008-5472.CAN-15-2402. [PubMed: 26896279]
23. Jacob F, Salinas RD, Zhang DY, Nguyen PTT, Schnoll JG, Wong SZH, Thokala R, Sheikh S, Saxena D, Prokop S, et al. (2020). A Patient-Derived Glioblastoma Organoid Model and Biobank Recapitulates Inter- and Intra-tumoral Heterogeneity. *Cell* 180, 188–204 e122. 10.1016/j.cell.2019.11.036. [PubMed: 31883794]
24. LeBlanc VG, Trinh DL, Aslanpour S, Hughes M, Livingstone D, Jin D, Ahn BY, Blough MD, Cairncross JG, Chan JA, et al. (2022). Single-cell landscapes of primary glioblastomas and matched explants and cell lines show variable retention of inter- and intratumor heterogeneity. *Cancer Cell* 40, 379–392 e379. 10.1016/j.ccell.2022.02.016. [PubMed: 35303420]
25. Ben-Porath I, Thomson MW, Carey VJ, Ge R, Bell GW, Regev A, and Weinberg RA (2008). An embryonic stem cell-like gene expression signature in poorly differentiated aggressive human tumors. *Nat Genet* 40, 499–507. 10.1038/ng.127. [PubMed: 18443585]
26. Neftel C, Laffy J, Filbin MG, Hara T, Shore ME, Rahme GJ, Richman AR, Silverbush D, Shaw ML, Hebert CM, et al. (2019). An Integrative Model of Cellular States, Plasticity, and Genetics for Glioblastoma. *Cell* 178, 835–849 e821. 10.1016/j.cell.2019.06.024. [PubMed: 31327527]
27. Suva ML, Rheinbay E, Gillespie SM, Patel AP, Wakimoto H, Rabkin SD, Riggi N, Chi AS, Cahill DP, Nahed BV, et al. (2014). Reconstructing and reprogramming the tumor-propagating potential of glioblastoma stem-like cells. *Cell* 157, 580–594. 10.1016/j.cell.2014.02.030. [PubMed: 24726434]
28. Ding Y, Hubert CG, Herman J, Corrin P, Toledo CM, Skutt-Kakaria K, Vazquez J, Basom R, Zhang B, Risler JK, et al. (2013). Cancer-Specific requirement for BUB1B/BUBR1 in human brain tumor isolates and genetically transformed cells. *Cancer Discov* 3, 198–211. 10.1158/2159-8290.CD-12-0353. [PubMed: 23154965]
29. Zhang N, Wei P, Gong A, Chiu WT, Lee HT, Colman H, Huang H, Xue J, Liu M, Wang Y, et al. (2011). FoxM1 promotes beta-catenin nuclear localization and controls Wnt target-gene expression and glioma tumorigenesis. *Cancer Cell* 20, 427–442. 10.1016/j.ccr.2011.08.016. [PubMed: 22014570]
30. Bhang HE, Ruddy DA, Krishnamurthy Radhakrishna V, Caushi JX, Zhao R, Hims MM, Singh AP, Kao I, Rakiec D, Shaw P, et al. (2015). Studying clonal dynamics in response to cancer therapy using high-complexity barcoding. *Nat Med* 21, 440–448. 10.1038/nm.3841. [PubMed: 25849130]
31. Greaves M, and Maley CC (2012). Clonal evolution in cancer. *Nature* 481, 306–313. 10.1038/nature10762. [PubMed: 22258609]
32. Reya T, Morrison SJ, Clarke MF, and Weissman IL (2001). Stem cells, cancer, and cancer stem cells. *Nature* 414, 105–111. 10.1038/35102167. [PubMed: 11689955]
33. Bleau AM., Hambarzumyan D., Ozawa T., Fomchenko EI., Huse JT., Brennan CW., and Holland EC. (2009). PTEN/PI3K/Akt pathway regulates the side population phenotype and ABCG2 activity in glioma tumor stem-like cells. *Cell Stem Cell* 4, 226–235. 10.1016/j.stem.2009.01.007. [PubMed: 19265662]

34. Minata M, Audia A, Shi J, Lu S, Bernstock J, Pavlyukov MS, Das A, Kim SH, Shin YJ, Lee Y, et al. (2019). Phenotypic Plasticity of Invasive Edge Glioma Stem-like Cells in Response to Ionizing Radiation. *Cell Rep* 26, 1893–1905 e1897. 10.1016/j.celrep.2019.01.076. [PubMed: 30759398]
35. Morrissey JH, Fakhrai H, and Edgington TS (1987). Molecular cloning of the cDNA for tissue factor, the cellular receptor for the initiation of the coagulation protease cascade. *Cell* 50, 129–135. 10.1016/0092-8674(87)90669-6. [PubMed: 3297348]
36. Rao LV, and Rapaport SI (1988). Activation of factor VII bound to tissue factor: a key early step in the tissue factor pathway of blood coagulation. *Proc Natl Acad Sci U S A* 85, 6687–6691. [PubMed: 3261869]
37. Mackman N (2004). Role of tissue factor in hemostasis, thrombosis, and vascular development. *Arterioscler Thromb Vasc Biol* 24, 1015–1022. 10.1161/01.ATV.0000130465.23430.74. [PubMed: 15117736]
38. Cimmino G, and Cirillo P (2018). Tissue factor: newer concepts in thrombosis and its role beyond thrombosis and hemostasis. *Cardiovasc Diagn Ther* 8, 581–593. 10.21037/cdt.2018.10.14. [PubMed: 30498683]
39. van den Berg YW, Osanto S, Reitsma PH, and Versteeg HH (2012). The relationship between tissue factor and cancer progression: insights from bench and bedside. *Blood* 119, 924–932. 10.1182/blood-2011-06-317685. [PubMed: 22065595]
40. Bourcy M, Suarez-Carmona M, Lambert J, Francart ME, Schroeder H, Delierneux C, Skrypek N, Thompson EW, Jerusalem G, Berx G, et al. (2016). Tissue Factor Induced by Epithelial-Mesenchymal Transition Triggers a Procoagulant State That Drives Metastasis of Circulating Tumor Cells. *Cancer Res* 76, 4270–4282. 10.1158/0008-5472.CAN-15-2263. [PubMed: 27221703]
41. Unruh D, Mirkov S, Wray B, Drumm M, Lamano J, Li YD, Haider QF, Javier R, McCortney K, Saratsis A, et al. (2019). Methylation-dependent Tissue Factor Suppression Contributes to the Reduced Malignancy of IDH1-mutant Gliomas. *Clin Cancer Res* 25, 747–759. 10.1158/1078-0432.CCR-18-1222. [PubMed: 30266764]
42. Xie XP, Laks DR, Sun D, Ganbold M, Wang Z, Pedraza AM, Bale T, Tabar V, Brennan C, Zhou X, and Parada LF (2022). Quiescent human glioblastoma cancer stem cells drive tumor initiation, expansion, and recurrence following chemotherapy. *Dev Cell* 57, 32–46 e38. 10.1016/j.devcel.2021.12.007. [PubMed: 35016005]
43. Baar MP, Brandt RMC, Putavet DA, Klein JDD, Derks KWJ, Bourgeois BRM, Stryeck S, Rijkse Y, van Willigenburg H, Feijtel DA, et al. (2017). Targeted Apoptosis of Senescent Cells Restores Tissue Homeostasis in Response to Chemotoxicity and Aging. *Cell* 169, 132–147 e116. 10.1016/j.cell.2017.02.031. [PubMed: 28340339]
44. Kurppa KJ, Liu Y, To C, Zhang T, Fan M, Vajdi A, Knelson EH, Xie Y, Lim K, Cejas P, et al. (2020). Treatment-Induced Tumor Dormancy through YAP-Mediated Transcriptional Reprogramming of the Apoptotic Pathway. *Cancer Cell* 37, 104–122 e112. 10.1016/j.ccell.2019.12.006. [PubMed: 31935369]
45. Carro MS, Lim WK, Alvarez MJ, Bollo RJ, Zhao X, Snyder EY, Sulman EP, Anne SL, Doetsch F, Colman H, et al. (2010). The transcriptional network for mesenchymal transformation of brain tumours. *Nature* 463, 318–325. 10.1038/nature08712. [PubMed: 20032975]
46. Chien Y., Scuoppo C., Wang X., Fang X., Balgley B., Bolden JE., Premrurit P., Luo W., Chicas A., Lee CS., et al. (2011). Control of the senescence-associated secretory phenotype by NF-kappaB promotes senescence and enhances chemosensitivity. *Genes Dev* 25, 2125–2136. 10.1101/gad.17276711. [PubMed: 21979375]
47. Kim E, Kim M, Woo DH, Shin Y, Shin J, Chang N, Oh YT, Kim H, Rhee J, Nakano I, et al. (2013). Phosphorylation of EZH2 activates STAT3 signaling via STAT3 methylation and promotes tumorigenicity of glioblastoma stem-like cells. *Cancer Cell* 23, 839–852. 10.1016/j.ccr.2013.04.008. [PubMed: 23684459]
48. Prager BC, Bhargava S, Mahadev V, Hubert CG, and Rich JN (2020). Glioblastoma Stem Cells: Driving Resilience through Chaos. *Trends Cancer* 6, 223–235. 10.1016/j.trecan.2020.01.009. [PubMed: 32101725]

49. Aldape K, Brindle KM, Chesler L, Chopra R, Gajjar A, Gilbert MR, Gottardo N, Gutmann DH, Hargrave D, Holland EC, et al. (2019). Challenges to curing primary brain tumours. *Nat Rev Clin Oncol* 16, 509–520. 10.1038/s41571-019-0177-5. [PubMed: 30733593]
50. Wang Q, Hu B, Hu X, Kim H, Squatrito M, Scarpace L, deCarvalho AC, Lyu S, Li P, Li Y, et al. (2017). Tumor Evolution of Glioma-Intrinsic Gene Expression Subtypes Associates with Immunological Changes in the Microenvironment. *Cancer Cell* 32, 42–56 e46. 10.1016/j.ccell.2017.06.003. [PubMed: 28697342]
51. Phillips HS, Kharbanda S, Chen R, Forrest WF, Soriano RH, Wu TD, Misra A, Nigro JM, Colman H, Soroceanu L, et al. (2006). Molecular subclasses of high-grade glioma predict prognosis, delineate a pattern of disease progression, and resemble stages in neurogenesis. *Cancer Cell* 9, 157–173. 10.1016/j.ccr.2006.02.019. [PubMed: 16530701]
52. Galmiche A, Rak J, Roumenina LT, and Saidak Z (2022). Coagulome and the tumor microenvironment: an actionable interplay. *Trends Cancer*. 10.1016/j.trecan.2021.12.008.
53. Hambardzumyan D, Amankulor NM, Helmy KY, Becher OJ, and Holland EC (2009). Modeling Adult Gliomas Using RCAS/t-va Technology. *Transl Oncol* 2, 89–95. 10.1593/tlo.09100. [PubMed: 19412424]
54. Koren HS, Anderson SJ, and Larrick JW (1979). In vitro activation of a human macrophage-like cell line. *Nature* 279, 328–331. 10.1038/279328a0. [PubMed: 450085]
55. Ettelaie C, Collier ME, Featherby S, Greenman J, and Maraveyas A (2016). Oligoubiquitination of tissue factor on Lys255 promotes Ser253-dephosphorylation and terminates TF release. *Biochim Biophys Acta* 1863, 2846–2857. 10.1016/j.bbamcr.2016.09.005. [PubMed: 27599717]
56. Arvanitis CD, Ferraro GB, and Jain RK (2020). The blood-brain barrier and blood-tumour barrier in brain tumours and metastases. *Nat Rev Cancer* 20, 26–41. 10.1038/s41568-019-0205-x. [PubMed: 31601988]
57. Bago JR, Okolie O, Dumitru R, Ewend MG, Parker JS, Werff RV, Underhill TM, Schmid RS, Miller CR, and Hingtgen SD (2017). Tumor-homing cytotoxic human induced neural stem cells for cancer therapy. *Sci Transl Med* 9. 10.1126/scitranslmed.aah6510.
58. Kauer TM, Figueiredo JL, Hingtgen S, and Shah K (2011). Encapsulated therapeutic stem cells implanted in the tumor resection cavity induce cell death in gliomas. *Nat Neurosci* 15, 197–204. 10.1038/nn.3019. [PubMed: 22197831]
59. Varn FS, Johnson KC, Martinek J, Huse JT, Nasrallah MP, Wesseling P, Cooper LAD, Malta TM, Wade TE, Sabedot TS, et al. (2022). Glioma progression is shaped by genetic evolution and microenvironment interactions. *Cell* 185, 2184–2199 e2116. 10.1016/j.cell.2022.04.038. [PubMed: 35649412]
60. Coppe JP, Patil CK., Rodier F., Sun Y., Munoz DP., Goldstein J., Nelson PS., Desprez PY., and Campisi J. (2008). Senescence-associated secretory phenotypes reveal cell-nonautonomous functions of oncogenic RAS and the p53 tumor suppressor. *PLoS Biol* 6, 2853–2868. 10.1371/journal.pbio.0060301. [PubMed: 19053174]
61. Fridman AL, and Tainsky MA (2008). Critical pathways in cellular senescence and immortalization revealed by gene expression profiling. *Oncogene* 27, 5975–5987. 10.1038/onc.2008.213. [PubMed: 18711403]
62. Brennan CW, Verhaak RG, McKenna A, Campos B, Noushmehr H, Salama SR, Zheng S, Chakravarty D, Sanborn JZ, Berman SH, et al. (2013). The somatic genomic landscape of glioblastoma. *Cell* 155, 462–477. 10.1016/j.cell.2013.09.034. [PubMed: 24120142]
63. Liau BB, Sievers C, Donohue LK, Gillespie SM, Flavahan WA, Miller TE, Venteicher AS, Hebert CH, Carey CD, Rodig SJ, et al. (2017). Adaptive Chromatin Remodeling Drives Glioblastoma Stem Cell Plasticity and Drug Tolerance. *Cell Stem Cell* 20, 233–246 e237. 10.1016/j.stem.2016.11.003. [PubMed: 27989769]
64. Milanovic M, Fan DNY, Belenki D, Dabritz JHM, Zhao Z, Yu Y, Dorr JR, Dimitrova L, Lenze D, Monteiro Barbosa IA, et al. (2018). Senescence-associated reprogramming promotes cancer stemness. *Nature* 553, 96–100. 10.1038/nature25167. [PubMed: 29258294]
65. Collado M, Gil J, Efeyan A, Guerra C, Schuhmacher AJ, Barradas M, Benguria A, Zaballos A, Flores JM, Barbacid M, et al. (2005). Tumour biology: senescence in premalignant tumours. *Nature* 436, 642. 10.1038/436642a. [PubMed: 16079833]

66. Prasanna PG, Citrin DE, Hildesheim J, Ahmed MM, Venkatachalam S, Riscuta G, Xi D, Zheng G, Deursen JV, Goronzy J, et al. (2021). Therapy-Induced Senescence: Opportunities to Improve Anticancer Therapy. *J Natl Cancer Inst* 113, 1285–1298. 10.1093/jnci/djab064. [PubMed: 33792717]
67. Trousseau A (1865). Phlegmasia alba dolens. *Clinique medicule de l'Hotel-Dieu de Paris* 3, 94.
68. Saidak Z, Soudet S, Lottin M, Salle V, Sevestre MA, Clatot F, and Galmiche A (2021). A pan-cancer analysis of the human tumor coagulome and its link to the tumor immune microenvironment. *Cancer Immunol Immunother* 70, 923–933. 10.1007/s00262-020-02739-w. [PubMed: 33057845]
69. Morrow JJ, Bayles I, Funnell APW, Miller TE, Saiakhova A, Lizardo MM, Bartels CF, Kapteijn MY, Hung S, Mendoza A, et al. (2018). Positively selected enhancer elements endow osteosarcoma cells with metastatic competence. *Nat Med* 24, 176–185. 10.1038/nm.4475. [PubMed: 29334376]
70. Feinauer MJ, Schneider SW, Berghoff AS, Robador JR, Tehranian C, Karreman MA, Venkataramani V, Solecki G, Grosch JK, Gunkel K, et al. (2021). Local blood coagulation drives cancer cell arrest and brain metastasis in a mouse model. *Blood* 137, 1219–1232. 10.1182/blood.2020005710. [PubMed: 33270819]
71. Wiley CD., Liu S., Limbad C., Zawadzka AM., Beck J., Demaria M., Artwood R., Alimirah F., Lopez-Dominguez JA., Kuehnemann C., et al. (2019). SILAC Analysis Reveals Increased Secretion of Hemostasis-Related Factors by Senescent Cells. *Cell Rep* 28, 3329–3337 e3325. 10.1016/j.celrep.2019.08.049. [PubMed: 31553904]
72. Lee S, Yu Y, Trimpert J, Benthani F, Mairhofer M, Richter-Pechanska P, Wyler E, Belenki D, Kaltenbrunner S, Pammer M, et al. (2021). Virus-induced senescence is a driver and therapeutic target in COVID-19. *Nature* 599, 283–289. 10.1038/s41586-021-03995-1. [PubMed: 34517409]
73. Moiseeva V, Cisneros A, Sica V, Deryagin O, Lai Y, Jung S, Andres E, An J, Segales J, Ortet L, et al. (2023). Senescence atlas reveals an aged-like inflamed niche that blunts muscle regeneration. *Nature* 613, 169–178. 10.1038/s41586-022-05535-x. [PubMed: 36544018]
74. Nguyen D, Jeon HM, and Lee J (2022). Tissue factor links inflammation, thrombosis, and senescence in COVID-19. *Sci Rep* 12, 19842. 10.1038/s41598-022-23950-y. [PubMed: 36400883]
75. Birch J, and Gil J (2020). Senescence and the SASP: many therapeutic avenues. *Genes Dev* 34, 1565–1576. 10.1101/gad.343129.120. [PubMed: 33262144]
76. Dou Z, Ghosh K, Vizioli MG, Zhu J, Sen P, Wangenstein KJ, Simithy J, Lan Y, Lin Y, Zhou Z, et al. (2017). Cytoplasmic chromatin triggers inflammation in senescence and cancer. *Nature* 550, 402–406. 10.1038/nature24050. [PubMed: 28976970]
77. Wang C, Vegna S, Jin H, Benedict B, Lieftink C, Ramirez C, de Oliveira RL, Morris B, Gadiot J, Wang W, et al. (2019). Inducing and exploiting vulnerabilities for the treatment of liver cancer. *Nature* 574, 268–272. 10.1038/s41586-019-1607-3. [PubMed: 31578521]
78. Amor C, Feucht J, Leibold J, Ho YJ, Zhu C, Alonso-Curbelo D, Mansilla-Soto J, Boyer JA, Li X, Giavridis T, et al. (2020). Senolytic CAR T cells reverse senescence-associated pathologies. *Nature* 583, 127–132. 10.1038/s41586-020-2403-9. [PubMed: 32555459]
79. Coppe JP, Desprez PY, Krtolica A, and Campisi J (2010). The senescence-associated secretory phenotype: the dark side of tumor suppression. *Annu Rev Pathol* 5, 99–118. 10.1146/annurev-pathol-121808-102144. [PubMed: 20078217]
80. Faget DV, Ren Q, and Stewart SA (2019). Unmasking senescence: context-dependent effects of SASP in cancer. *Nat Rev Cancer* 19, 439–453. 10.1038/s41568-019-0156-2. [PubMed: 31235879]
81. Wang B, Kohli J, and Demaria M (2020). Senescent Cells in Cancer Therapy: Friends or Foes? *Trends Cancer*. 10.1016/j.trecan.2020.05.004.
82. De Palma M, and Lewis CE (2013). Macrophage regulation of tumor responses to anticancer therapies. *Cancer Cell* 23, 277–286. 10.1016/j.ccr.2013.02.013. [PubMed: 23518347]
83. DeNardo DG, and Ruffell B (2019). Macrophages as regulators of tumour immunity and immunotherapy. *Nat Rev Immunol* 19, 369–382. 10.1038/s41577-019-0127-6. [PubMed: 30718830]
84. Lee J, Kotliarova S, Kotliarov Y, Li A, Su Q, Donin NM, Pastorino S, Purow BW, Christopher N, Zhang W, et al. (2006). Tumor stem cells derived from glioblastomas cultured in bFGF and EGF

- more closely mirror the phenotype and genotype of primary tumors than do serum-cultured cell lines. *Cancer Cell* 9, 391–403. 10.1016/j.ccr.2006.03.030. [PubMed: 16697959]
85. Pine AR, Cirigliano SM, Nicholson JG, Hu Y, Linkous A, Miyaguchi K, Edwards L, Singhanian R, Schwartz TH, Ramakrishna R, et al. (2020). Tumor Microenvironment Is Critical for the Maintenance of Cellular States Found in Primary Glioblastomas. *Cancer Discov* 10, 964–979. 10.1158/2159-8290.CD-20-0057. [PubMed: 32253265]
86. Mathieu V, De Neve N, Le Mercier M, Dewelle J, Gaussin JF, Dehoux M, Kiss R, and Lefranc F (2008). Combining bevacizumab with temozolomide increases the antitumor efficacy of temozolomide in a human glioblastoma orthotopic xenograft model. *Neoplasia* 10, 1383–1392. 10.1593/neo.08928. [PubMed: 19048117]
87. Brake MA, Ivanciu L, Maroney SA, Martinez ND, Mast AE, and Westrick RJ (2019). Assessing Blood Clotting and Coagulation Factors in Mice. *Curr Protoc Mouse Biol* 9, e61. 10.1002/cpmo.61. [PubMed: 30875463]
88. Verhaak RG., Hoadley KA., Purdom E., Wang V., Qi Y., Wilkerson MD., Miller CR., Ding L., Golub T., Mesirov JP., et al. (2010). Integrated genomic analysis identifies clinically relevant subtypes of glioblastoma characterized by abnormalities in PDGFRA, IDH1, EGFR, and NF1. *Cancer Cell* 17, 98–110. 10.1016/j.ccr.2009.12.020. [PubMed: 20129251]
89. Tasdemir N, Banito A, Roe JS, Alonso-Curbelo D, Camiolo M, Tschaharganeh DF, Huang CH, Aksoy O, Bolden JE, Chen CC, et al. (2016). BRD4 Connects Enhancer Remodeling to Senescence Immune Surveillance. *Cancer Discov* 6, 612–629. 10.1158/2159-8290.CD-16-0217. [PubMed: 27099234]
90. Eckel-Passow JE, Lachance DH, Molinaro AM, Walsh KM, Decker PA, Sicotte H, Pekmezci M, Rice T, Kosel ML, Smirnov IV, et al. (2015). Glioma Groups Based on 1p/19q, IDH, and TERT Promoter Mutations in Tumors. *N Engl J Med* 372, 2499–2508. 10.1056/NEJMoa1407279. [PubMed: 26061753]
91. Mercurio F, Zhu H, Murray BW, Shevchenko A, Bennett BL, Li J, Young DB, Barbosa M, Mann M, Manning A, and Rao A (1997). IKK-1 and IKK-2: cytokine-activated IκB kinases essential for NF-κB activation. *Science* 278, 860–866. 10.1126/science.278.5339.860. [PubMed: 9346484]
92. Toso R, Pinotti M, High KA, Pollak ES, and Bernardi F (2002). A frequent human coagulation Factor VII mutation (A294V, c152) in loop 140s affects the interaction with activators, tissue factor and substrates. *Biochem J* 363, 411–416. 10.1042/0264-6021:3630411. [PubMed: 11931672]
93. Subramanian A, Tamayo P, Mootha VK, Mukherjee S, Ebert BL, Gillette MA, Paulovich A, Pomeroy SL, Golub TR, Lander ES, and Mesirov JP (2005). Gene set enrichment analysis: a knowledge-based approach for interpreting genome-wide expression profiles. *Proc Natl Acad Sci U S A* 102, 15545–15550. 10.1073/pnas.0506580102. [PubMed: 16199517]
94. Wolf FA, Angerer P, and Theis FJ (2018). SCANPY: large-scale single-cell gene expression data analysis. *Genome Biol* 19, 15. 10.1186/s13059-017-1382-0. [PubMed: 29409532]
95. Becht E, McInnes L, Healy J, Dutertre CA, Kwok IWH, Ng LG, Ginhoux F, and Newell EW (2018). Dimensionality reduction for visualizing single-cell data using UMAP. *Nat Biotechnol*. 10.1038/nbt.4314.

Highlights

- Irradiated SA- β Gal⁺ GBM cells clonally expand and promote post-RT tumor regrowth.
- RT-induced F3 signaling enhances the enriched features of senescence and stemness.
- F3 is a key driver for oncogenic ECM and TME remodeling in GBM radio-resistance.
- FVII is a potent anti-GBM agent that mitigates F3-mediated oncogenic signaling.

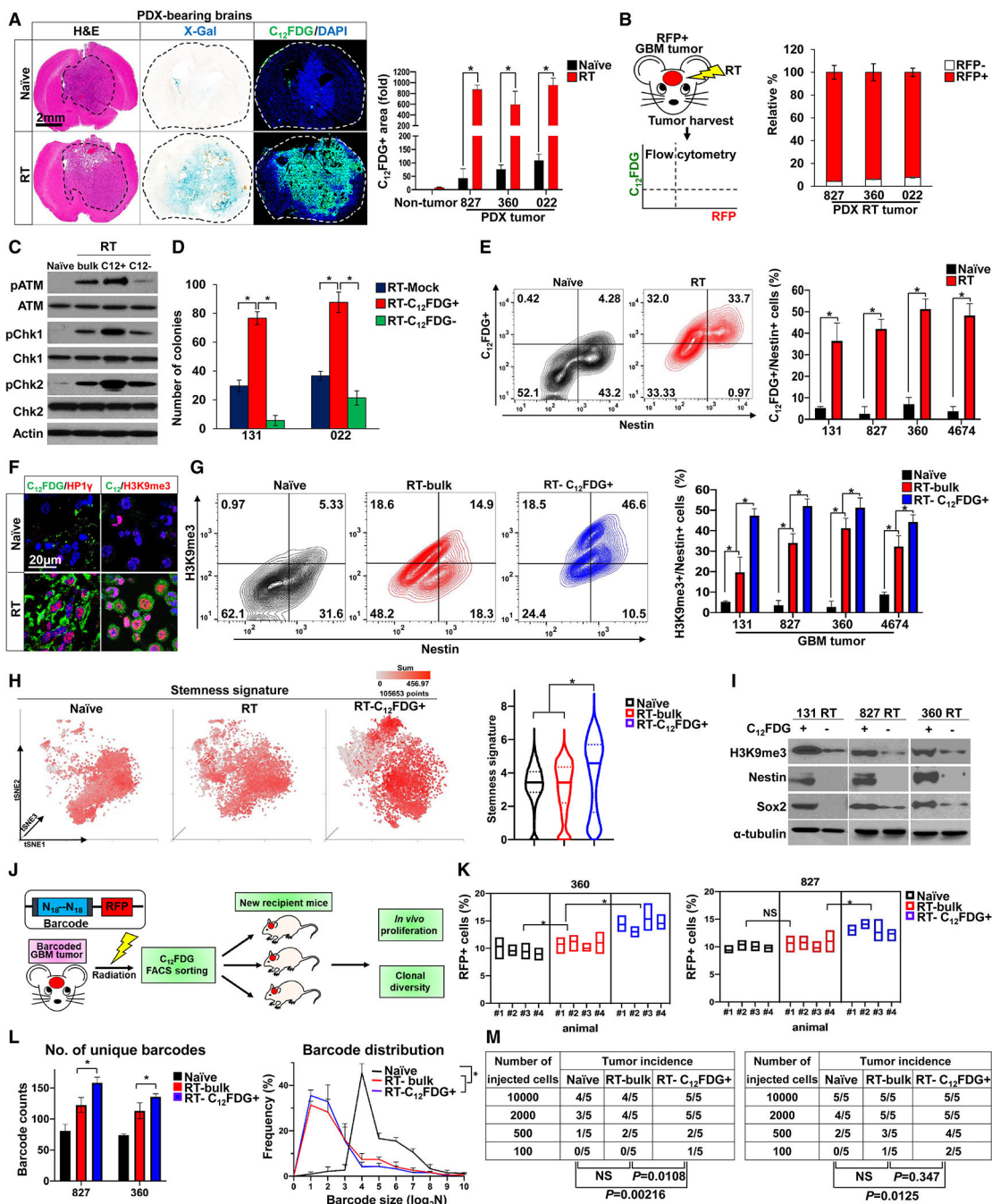


Figure 1. Radiation-induced SA-βGal⁺ GBM cells clonally expand *in vivo*.

(A) Representative images of SA-βGal activity in the brain sections. GBM tumor-bearing mice were not irradiated or irradiated (naïve and RT, respectively) and stained with X-gal or C₁₂FDG five days later. Tumor regions were shown in H&E images. Different patient-derived GBMs are designated as numbers. * p < 0.001 by one-way ANOVA.

(B) Proportion of RFP⁺ cells (human GBM cells) and RFP⁻ cells (mouse cells) within C₁₂FDG⁺ populations (n = 3 per each).

- (C) Immunoblots of DNA damage response (DDR) proteins in sorted RT-C₁₂FDG⁺ and C₁₂FDG⁻ GBM subpopulations. β -actin was used as a loading control.
- (D) *In vitro* clonogenic growth of irradiated GBM subpopulations. Single cells from each subpopulation were plated in soft agar, cultured for 3 weeks, and resultant colonies counted. * $p < 0.001$ by one-way ANOVA with Tukey's multiple comparison test.
- (E) Flow cytometry plot of C₁₂FDG and Nestin staining in naïve and RT GBM cells. Quantitation of C₁₂FDG⁺ / Nestin⁺ cells are shown. * $p < 0.001$ by one-way ANOVA.
- (F) Immunofluorescence (IF) staining images of C₁₂FDG and senescence markers (HP1 γ and H3K9me3).
- (G) Flow cytometry plot of H3K9me3 and Nestin staining in naïve, RT-bulk, and RT-C₁₂FDG⁺ GBM cells. * $p < 0.001$ by one-way ANOVA with Tukey's multiple comparison test.
- (H) t-distributed Stochastic Neighbor Embedding (t-SNE) plots of GBM single cells in the naïve, RT-bulk, and RT-C₁₂FDG⁺ GBM cells (total of 105,653 cells). Color gradient was overlaid with stemness signature scores. * $p < 0.001$ by Mann-Whitney test.
- (I) Immunoblots of H3K9me3 and GBM stemness markers (Nestin and Sox2) proteins in three matched sets of RT-C₁₂FDG⁺ and RT-C₁₂FDG⁻ GBM subpopulations.
- (J to L) Barcode-mediated clonal expansion and clonal diversity determination analysis. (J) Experimental schematic. (K) Floating bar plots of RFP-labeled cell populations *in vivo*. Center line in each bar represents mean value (n=4 animals per group). (L) Numbers of unique barcodes and barcode distribution within the tumors derived from the indicated cell populations. * $p < 0.01$ by two-way ANOVA. NS, not significant.
- (M) *In vivo* limiting dilution tumor formation results using naïve, RT-bulk, and RT-C₁₂FDG⁺ GBM cells. P values were determined by two-way ANOVA. Results are presented as mean \pm SD. See also Figure S1.

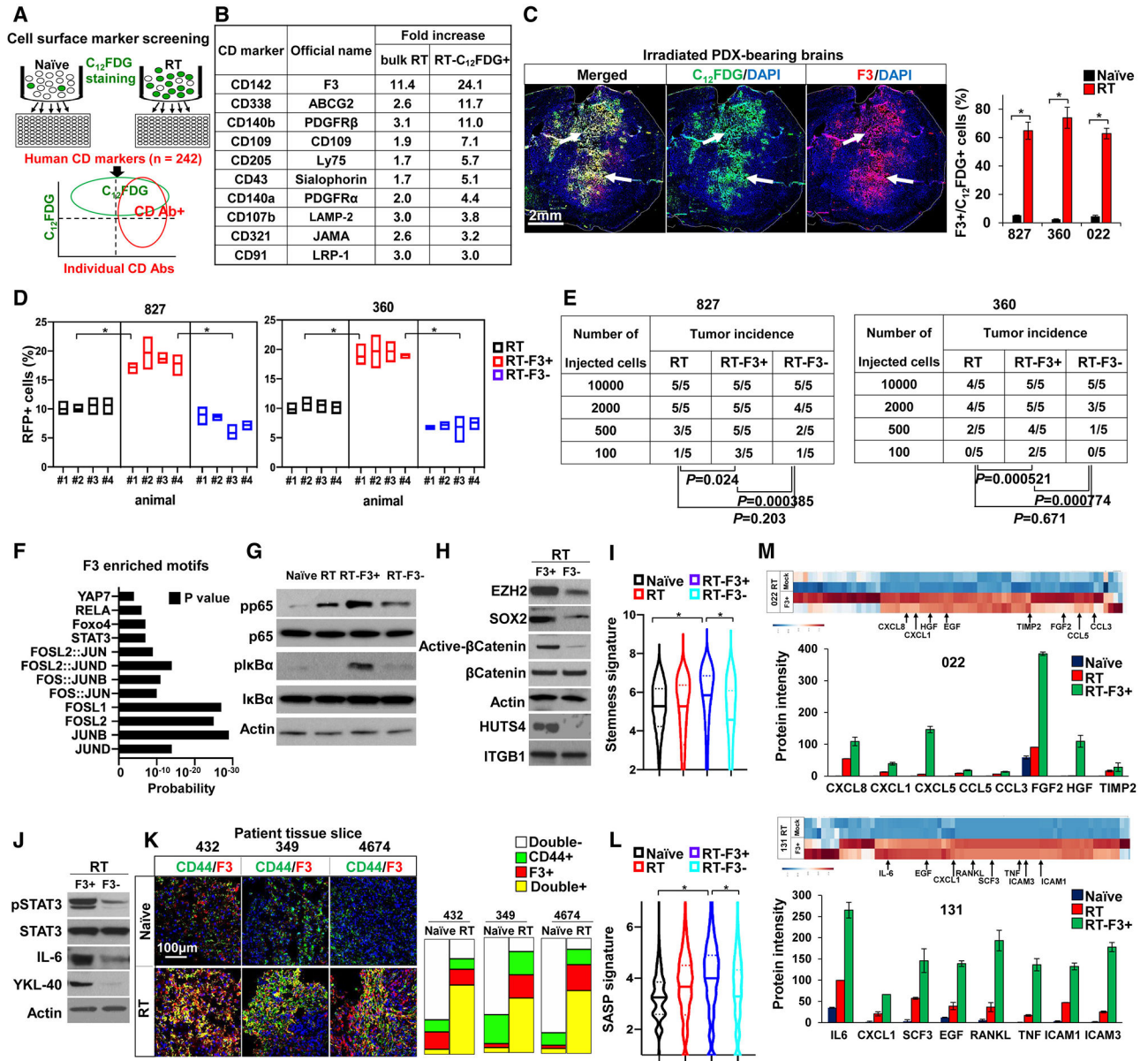


Figure 2. F3, highly expressed in irradiated C₁₂FDG⁺ GBM cells, is associated with stemness, cell state transition, and an enhanced secretory phenotype.

(A) A schematic of the cell surface marker screen. (B) The lists of the cell surface proteins that were enriched in RT-bulk and RT-C₁₂FDG⁺ GBM cells compared to naïve cells. (C) IF staining images of C₁₂FDG and F3 in the brains of PDX tumor-bearing mice. C₁₂FDG⁺/F3⁺ double-positive cells were quantitated (n=3 per each tumor). * p < 0.001 by one-way ANOVA.

(D and E) *In vivo* proliferation of RT bulk, RT-F3⁺, and RT-F3⁻ cell populations (D) and *in vivo* limiting dilution tumor formation results. * p < 0.01 by two-way ANOVA.

(F) Enriched transcription factor-binding motifs in RT-F3⁺ subpopulations, as determined by ATAC sequencing analysis.

(G and H) Immunoblots of pp65, pI κ B α , EZH2, active- β -catenin, Sox2, and HUTS4 proteins in the RT-F3⁺ and RT-F3⁻ GBM subpopulations. For detection with HUTS4 antibody (specific for the activated form of ITGB1), non-denaturing gels were used.

(I) Quantitation of stemness gene set expression in naïve, RT-bulk, RT-F3⁺, and RT-F3⁻ GBM single cells (total of 28,890 cells).

(J) Immunoblots of MES GBM transition-associated proteins (pSTAT3, IL6, and YKL-40).

(K) IF images of F3 and CD44 in matched naïve and irradiated GBM tissue slices and quantitation.

(L) Quantitation of SASP factor gene set expression in the above subpopulations.

(M) Heatmap plots and quantitation of the secreted proteins from naïve, RT-bulk, and RT-F3⁺ GBM cells. Results are mean \pm SD. * $p < 0.001$ by Mann-Whitney test in I and L. See also Figure S2 and Table S1.

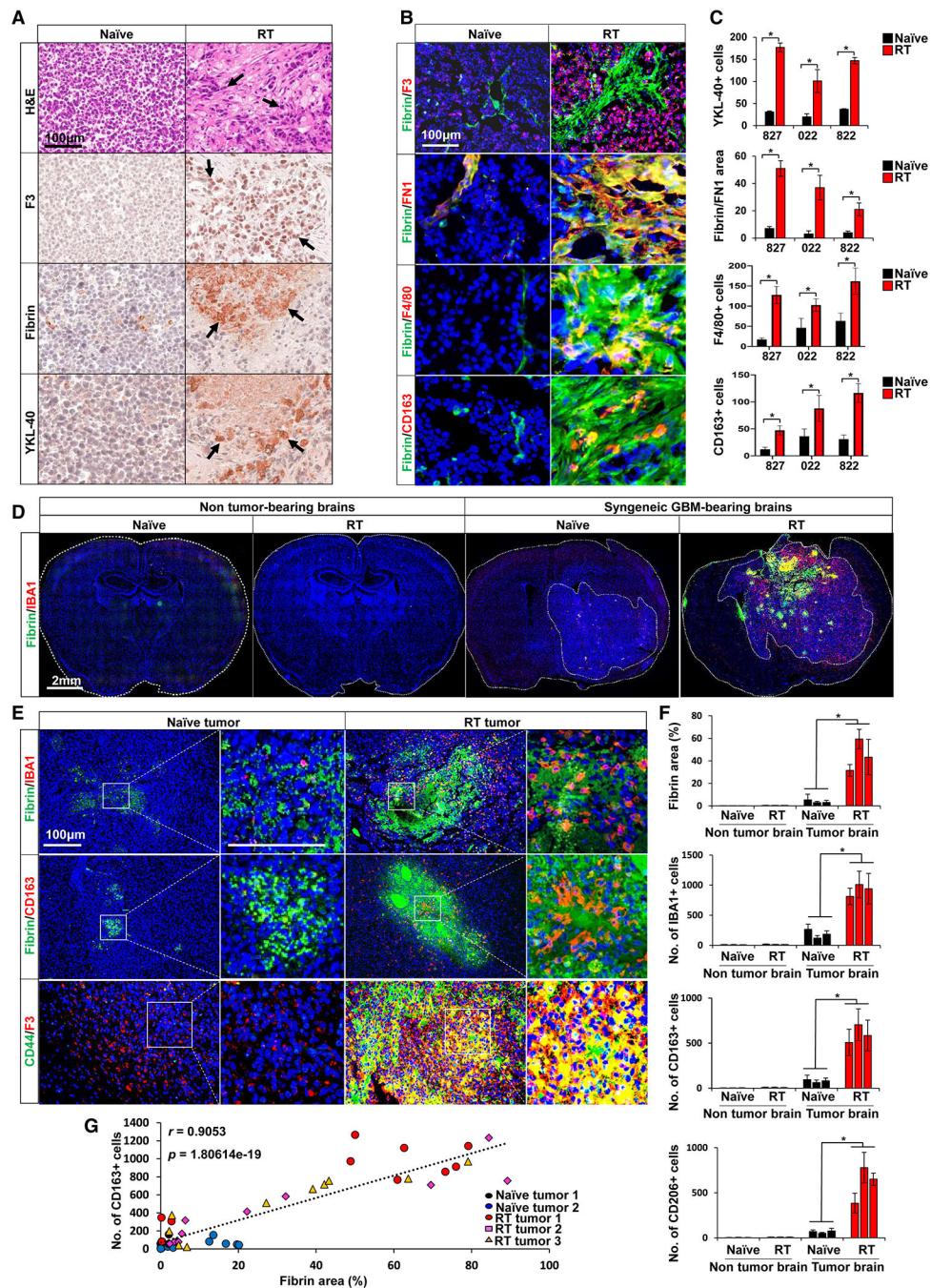


Figure 3. Radiation-induced F3 prime global changes both in tumor and microenvironment. (A) Immunohistochemical (IHC) staining images of F3, fibrin, and YKL-40 in 827 GBM tumors. Tumor-bearing mice were irradiated *in vivo* and tumors were harvested 5 days later. (B and C) IF images of fibrin, FN1 (an ECM molecule), F4/80, CD163 (M2-like TAM) staining. Fibrin⁺/FN1⁺ areas and numbers of YKL-40⁺, F4/80⁺, and CD163⁺ cells were quantitated (n = 4 per each). * p < 0.001 by one-way ANOVA. (D to F) IF images of fibrin, IBA1, CD163, CD44, F3 in syngeneic mouse gliomas and quantitation. * p < 0.001 by one-way ANOVA with Tukey's multiple comparison test.

(G) Correlation between the levels of fibrin polymers and CD163⁺ TAMs in the brain sections of tumor-bearing mice with or without RT. *r* value determined by Pearson's correlation coefficient analysis. Results are presented as mean ± SD. * *p* < 0.001. See also Figure S3.

Author Manuscript

Author Manuscript

Author Manuscript

Author Manuscript

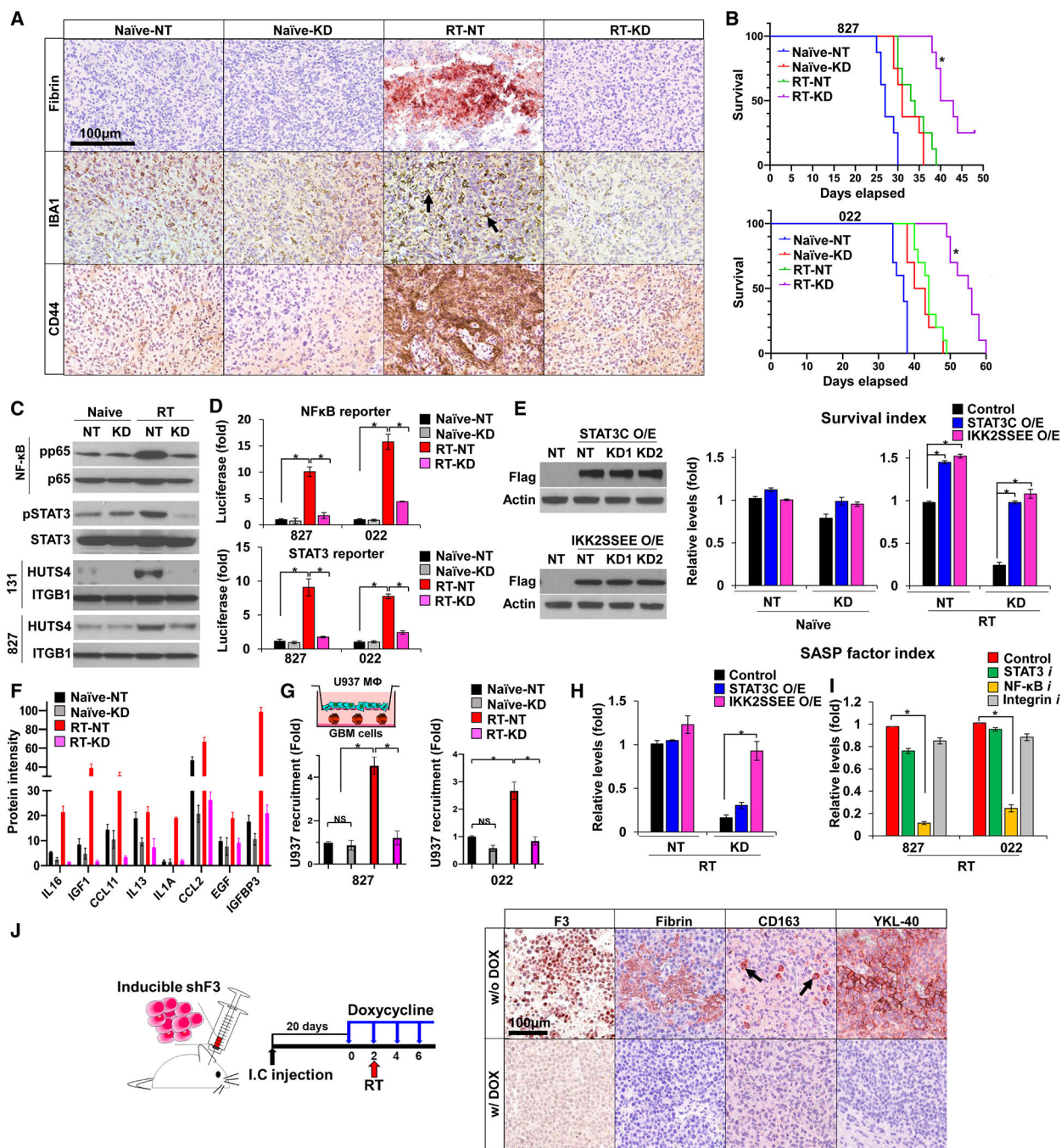


Figure 4. F3 knockdown suppresses radiation-induced coagulation, SASP factor secretion and TAM activation.

(A) IHC images of fibrin, IBA1, and CD44 in the brains of 827 tumors expressing either non-targeting (NT) or *F3* shRNAs (KD) with or without RT.

(B) Kaplan-Meier survival curves of mice in (A). n=8 for each group. $p < 0.001$ by log-rank analysis.

(C) Immunoblots to determine the activation status of NFκB and STAT3, and integrin in *F3* KD GBM cells with or without RT.

(D) Luciferase reporter assays to measure transcriptional activities of NF κ B and STAT3 signaling.

(E) Survival of irradiated *F3* KD cells with forced activation of STAT3 or NF κ B.

(F) Levels of the secreted proteins from GBM cells with or without *F3* KD and RT.

(G) Recruitment of macrophage (M ϕ)-like U937 cells co-cultured with the above cell groups.

(H and I) Levels of cytokine secretion in the cells with forced activation of STAT3 or NF κ B (H) or inhibition of NF κ B, STAT3, integrin signaling (I). Details of inhibitors are in Method section. SASP factor index is an arbitrary unit calculated from total amounts of the secreted proteins.

(J) IHC images of doxycycline-inducible *F3* shRNA expressing tumors. Tumors were harvested 7 days after doxycycline treatment. * $p < 0.001$ by one-way ANOVA with Tukey's multiple comparison test in D, E, G, H, and I. See also Figure S4.

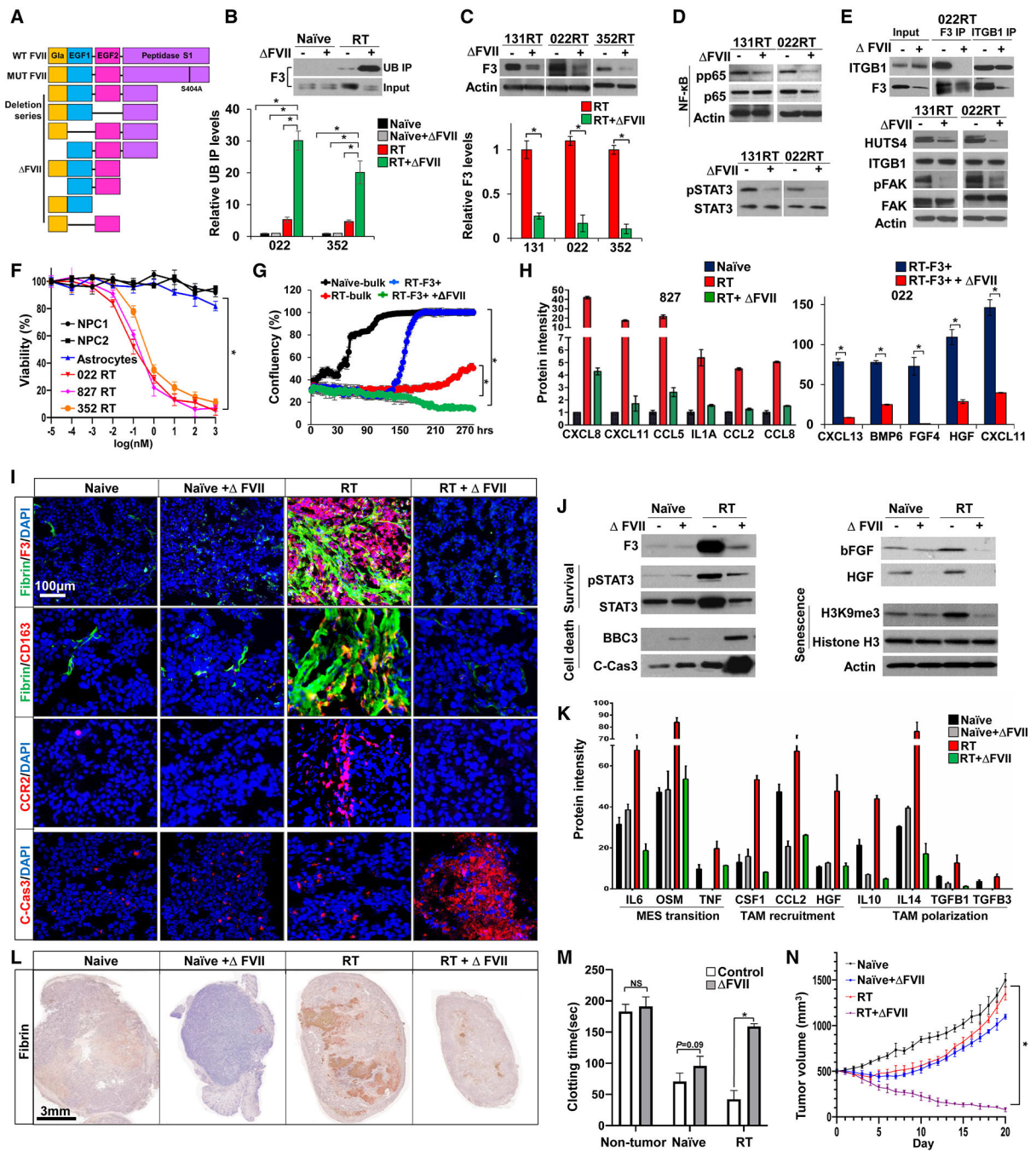


Figure 5. FVII treatment impeded RT-induced coagulation, SASP factor secretion, and TAM accumulation *in vivo*.

(A) Schematic of F7 deletion mutant structures.

(B) Co-immunoprecipitation (IP)-immunoblots of F3 and Ubiquitin (Ub) in naive and irradiated GBM cells treated with FVII recombinant protein for 1 day. Levels of ubiquitinated F3 proteins were quantitated by densitometry.

(C to E) Immunoblots of F3 (C), pp65 and pSTAT3 (D), and integrin signaling components (E) in irradiated GBM cells treated with FVII for 1 day. (E) Co-IP blots of F3-integrin β 1 (ITGB1) immunocomplexes.

- (F) Cell survival of normal brain cells and irradiated GBM cells treated with FVII. Irradiated GBM cells, NPCs, and astrocytes were cultured with various concentrations of FVII for 3 days and cell survival was determined by MTT assay.
- (G) Live-cell imaging of RT-F3⁺ 022 GBM cells treated with FVII. Cell growth was monitored in real-time over 12 days.
- (H) Quantitation of the secreted proteins using the conditioned media from irradiated GBM (022 and 827) cells treated with FVII for 1 day.
- (I) Representative staining images of fibrin, CD163, CCR2, and cleaved-caspase-3 (C-cas3) in the 827 GBM-derived PDX tumors treated with RT, FVII, or both.
- (J) Immunoblots of F3, pSTAT3, BBC3, C-cas3, bFGF, HGF, and H3K9me3 proteins using GBM tumor lysates.
- (K) Levels of the secreted proteins from the above tumor sets.
- (L) Tumor sizes and fibrin staining in the above tumor sets harvested 5 days after RT.
- (M) Tail bleeding times of tumor-bearing mice treated with RT, FVII, or both. n=3 for each group.
- (N) Tumor volumes of the above groups (n = 6). Results are presented as mean ± SD. * p < 0.001 by one-way ANOVA with Tukey's multiple comparison test in B, F, G and N. * p < 0.001 by one-way ANOVA in C, H, and M. See also Figure S5.

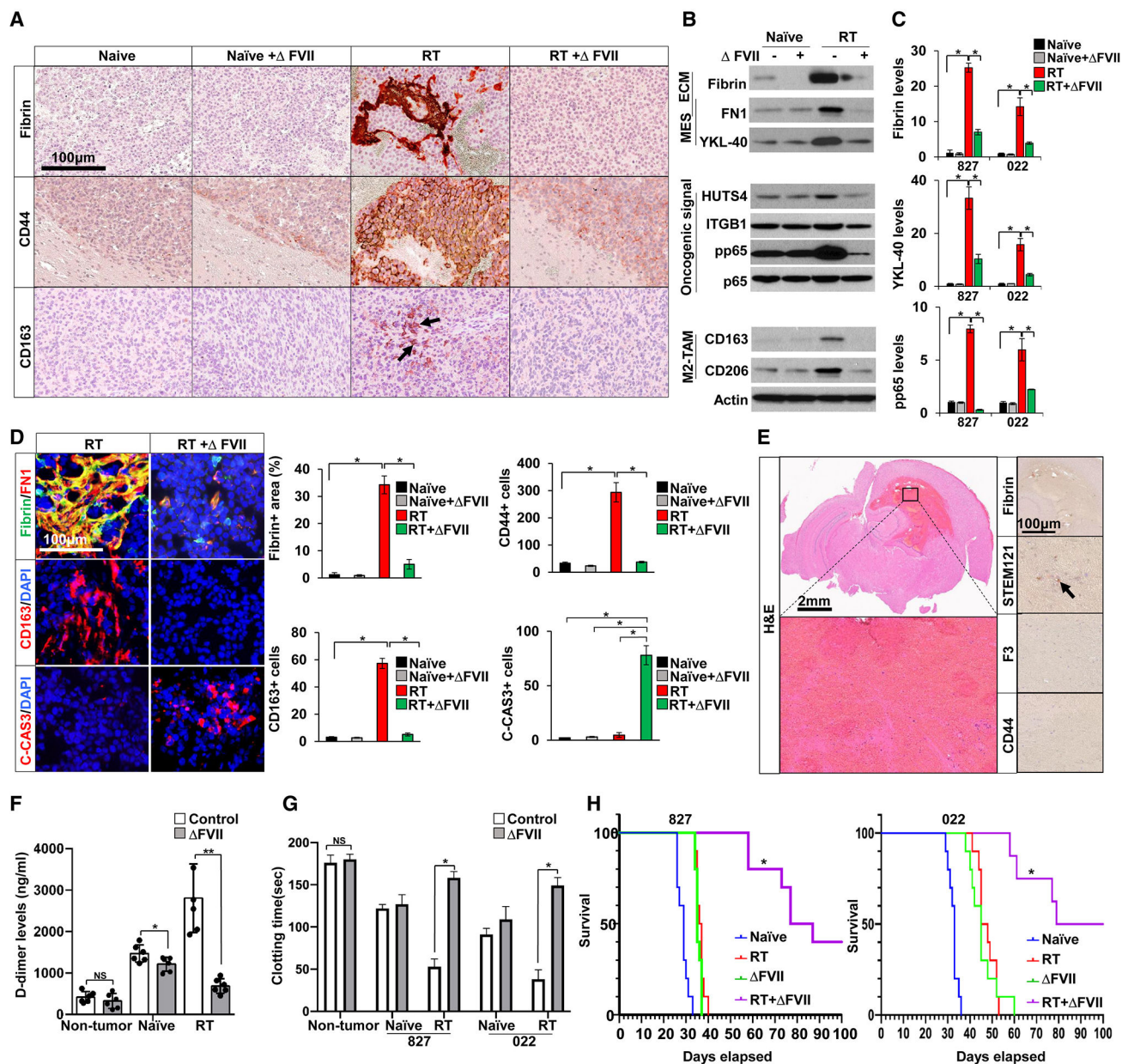


Figure 6. FVII therapies radio-sensitize GBM tumors in orthotopic PDX models.

(A) IHC images of fibrin, CD44, and CD163 in orthotopic 827 GBM tumor-bearing mice treated with RT, FVII, or both. Recombinant FVII protein (50 μ g/kg body weight) was administered via intravenous injection daily, concurrent with irradiation.

(B and C) Representative immunoblots of Fibrin, FN1, YKL-40, HSTS4, pp65, CD163, and CD206 in GBM tumors (B) and quantitation in (C).

(D) IF images of fibrin/FN1, CD44, CD163, and C-cas3 and quantitation. * $p < 0.001$ by one-way ANOVA with Tukey's multiple comparison test in C and D.

(E) H&E staining images of the mouse brain sections from combination treated group. Human tumor cells were stained with STEM121 antibody (human cell-specific marker).

(F and G) D-dimer levels in plasma (F) and tail bleeding time determination (G). N=3 for each group. * $p < 0.05$, ** $p < 0.001$ by one-way ANOVA in F. * $p < 0.001$ by one-way ANOVA in G.

(H) Kaplan-Meier survival curves of tumor bearing mice treated with radiation, FVII, or both. n=10 for each group. Combination-treated group showed a significant survival extension, compared to all other groups. $p < 0.001$ by log-rank analysis. See also Figure S6.

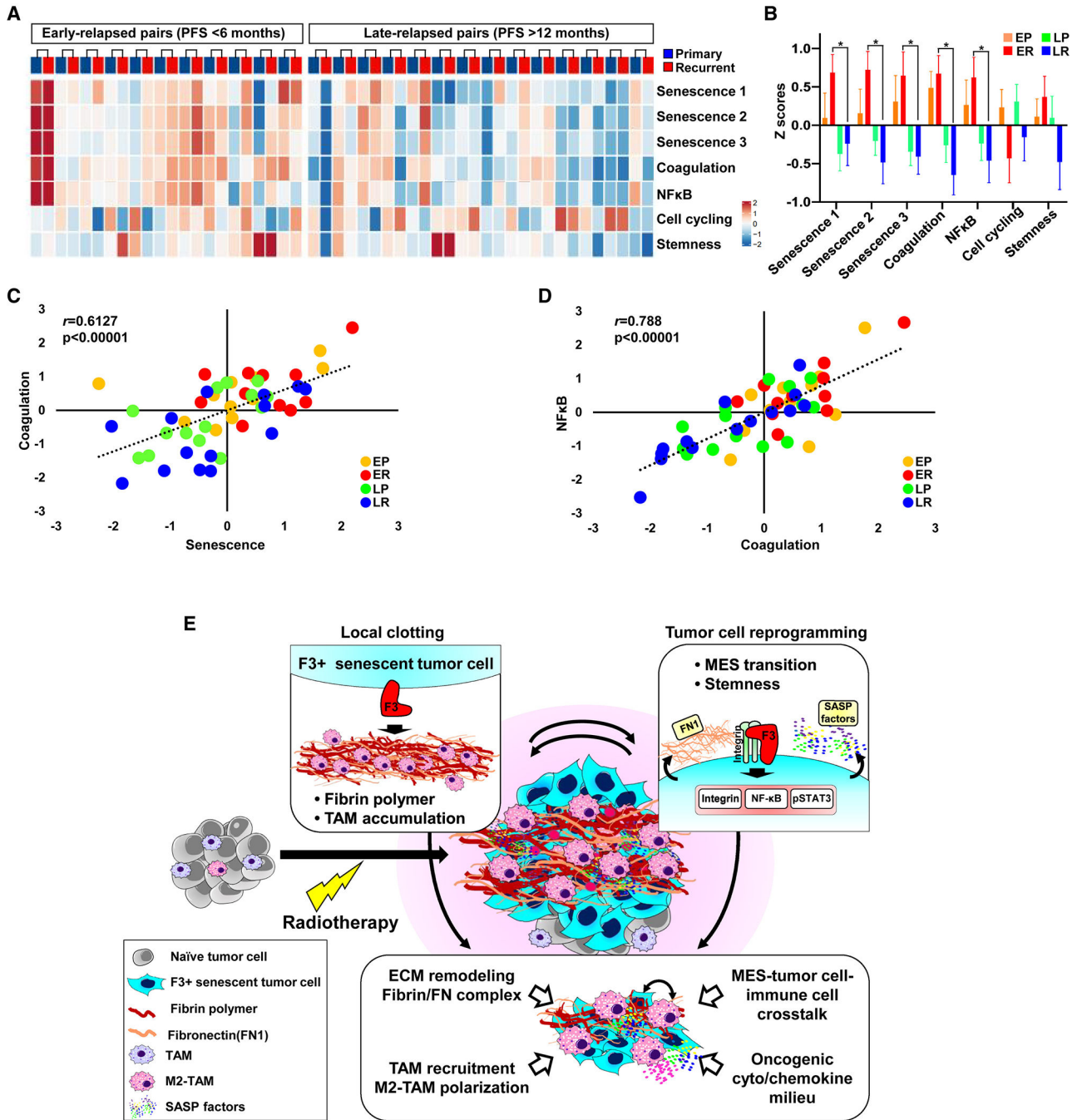


Figure 7. Expression of senescence and coagulation gene sets in matched primary and recurrent human GBM pairs.

(A) Heatmap plots of the senescence, coagulation, NFκB, cell cycling, and stemness gene set expression in early (n = 11) and late relapsed (n = 14) GBM pairs.

(B) Quantitation of each gene signature expression in the following tumor sets. EP, early-relapse GBM patients' primary tumors; ER, early-relapse GBM patients' recurrent tumors; LP, late-relapse GBM patients' primary tumors; LR, late-relapse GBM patients' recurrent tumors. Wilcoxon rank test and two-tailed Student's t test were performed. * p < 0.001.

(C and D) Scatter plot showing the correlations of coagulation and senescence signature gene expression (C), and NF κ B and coagulation (D). r values were determined by Pearson's correlation coefficient analysis.

(E) Schematic illustration to depict the roles of F3 signaling in RT-induced GBM remodeling. See also Figure S7.

Author Manuscript

Author Manuscript

Author Manuscript

Author Manuscript

KEY RESOURCES TABLE

REAGENT or RESOURCE	SOURCE	IDENTIFIER
Antibodies		
Mouse monoclonal anti-F3 (HTF-1)	BD Biosciences	Cat#55025; RRID: AB 393557
Mouse monoclonal anti-F3, Phycoerythrin Conjugated, (HTF-1)	BD Biosciences	Cat#550312; RRID: AB 393602
Rabbit polyclonal anti-F3	Abcam	Cat#ab104513; RRID: AB 10711603
Mouse monoclonal anti-F3 (10H10)	Invitrogen	Cat#MA1-83495; RRID: AB 2101347
Rabbit anti-phospho-ATM (Ser1981) (D6H9)	Cell Signaling	Cat#5883; RRID: AB 10835213
Rabbit anti-ATM (D2E2)	Cell Signaling	Cat#2873; RRID: AB 2062659
Rabbit anti-phospho-Chk1 (Ser345) (133D3)	Cell Signaling	Cat#2348; RRID: AB 331212
Mouse anti-Chk1 (2G1D5)	Cell Signaling	Cat#2360; RRID: AB 2080320
Rabbit anti-phospho-Chk2 (Thr68) (C13C1)	Cell Signaling	Cat#2197; RRID: AB 2080501
Rabbit anti-Chk2	Cell Signaling	Cat#2662; RRID: AB 2080793
Rabbit anti-Histone H3 (tri methyl K9)	Abcam	Cat#ab8898; RRID: AB 306848
Rabbit-anti-trimethyl-Histone H3 (Lys9)	Millipore Sigma	Cat#07-442; RRID: AB 310620
Mouse monoclonal anti-HP1 γ (14D3.1)	Millipore Sigma	Cat#MABE656; RRID: AB 2722628
Mouse monoclonal anti-PCNA	Santa Cruz Biotechnology	Cat#SC56; RRID: AB 628110
Monoclonal anti-Ki67 (MM1)	Leica Biosystems	Cat# NCL-L-Ki67-MM1; RRID:AB 563841
Goat polyclonal anti-Human Sox2	R&D systems	Cat#AF2018; RRID:AB 355110
Mouse monoclonal anti-Nestin (10c2)	Santa Cruz Biotechnology	Cat#SC-23927; RRID:AB 627994
Mouse anti-Human CD338 (ABCG2)	BD Biosciences	Cat#562167; RRID: AB 11153672
Mouse monoclonal anti-Fibrin (59D8)	Millipore Sigma	Cat#MAB52155; RRID: AB 2893306
Rabbit polyclonal anti-Fibronectin	Abcam	Cat#ab2413; RRID: AB 2262874
Mouse anti-Fibronectin	BD Biosciences	Cat#610077; RRID: AB 2105706
Rabbit polyclonal anti-CHI3L1	Abcam	Cat#ab77528; RRID:AB 2040911
Mouse monoclonal anti-CD44 (G44-26)	BD Biosciences	Cat#550392; RRID:AB 2074674
Rat monoclonal anti-CD44 (IM7)	Thermo Fisher Scientific	Cat#14044181; RRID:AB 467245
Rabbit monoclonal anti-Phospho-NF κ B p65 (Ser536) (93H1)	Cell Signaling	Cat#3033; RRID:AB 331284
Rabbit monoclonal Anti-NF κ B p65 (D14E12)	Cell Signaling	Cat#8242; RRID:AB 10859369

REAGENT or RESOURCE	SOURCE	IDENTIFIER
Mouse monoclonal Anti-phospho-IkBa (Ser32/36)(5A5)	Cell Signaling	Cat#9246; RRID:AB 2267145
Mouse monoclonal Anti-IkB-alpha (L35A5)	Cell Signaling	Cat#4814; RRID: AB 390781
Rabbit monoclonal anti-human beta-Catenin, phospho (Ser675) (D2F1)	Cell Signaling	Cat#4176; RRID:AB 1903923
Mouse monoclonal anti-Active-beta-catenin (8E7)	Millipore	Cat# 05-665; RRID:AB 309887
Mouse monoclonal anti-CD42b (42C01)	Thermo Fisher Scientific	Cat#MA5-11642; RRID:AB 10986763
Rabbit polyclonal anti-Histone H3 (CitH3)	Abcam	Cat#ab5103; RRID:AB 304752
Rat monoclonal anti-F4/80 (BM8)	Thermo Fisher Scientific	Cat#MF48000; RRID:AB 10376289
Rat monoclonal anti-CD163 (TNKUPJ)	Thermo Fisher Scientific	Cat#14163182; RRID:AB 2716934
Mouse monoclonal anti-CD163 (10D6)	Thermo Fisher Scientific	Cat#MA5-11458; RRID:AB 10982556
Rabbit recombinant CCR2 (EPR20844-15)	Abcam	Cat#ab273050; RRID: AB 2893307
Rat Monoclonal anti-CD11b	Abcam	Cat#ab8878; RRID:AB 306831
Rabbit polyclonal anti-Iba1	FUJIFILM Wako	Cat#019-19741; RRID:AB 839504
Rabbit polyclonal anti-Fibrinogen	Abcam	Cat#ab34269; RRID:AB 732367
Rabbit polyclonal anti-Ezh2 (D2C9)	Cell Signaling	Cat#5246; RRID:AB 10694683
Mouse monoclonal anti-Ubiquitin (P4D1):	Santa Cruz Biotechnology	Cat#SC8017; RRID: AB 628423
Rat monoclonal anti-Integrin β 1b (A1B2)	Sigma-Aldrich	Cat#MABT409; RRID:AB 2893323
Rabbit polyclonal anti-Integrin alpha 3	Abcam	Cat#ab131055; RRID:AB 11156484
Rabbit polyclonal anti-Integrin beta 1	Cell Signaling	Cat#4706; RRID:AB 823544
Goat Polyclonal anti-Human Integrin alpha 5 / cd49e	R&D systems	Cat#AF1864; RRID:AB 355026
Mouse monoclonal anti-Integrin beta 1 (HUTS4)	Millipore Sigma	Cat#MAB2079Z; RRID:AB 2233964
Mouse monoclonal anti-ITGB1 (TS2/16)	Thermo Fisher Scientific	Cat#MA2910; RRID:AB 223515
Mouse monoclonal anti-Integrin beta 1 [P5D2]	Abcam	Cat#ab24693; RRID: AB 448230
Rabbit monoclonal anti-pSTAT3(Tyr705) (D3A7)	Cell Signaling	Cat#9145; RRID:AB 2491009
Mouse monoclonal anti-Stat3 (124H6)	Cell Signaling	Cat#9139; RRID:AB 331757
Rabbit monoclonal anti-pAKT(S473) (D9E)	Cell Signaling	Cat#4060; RRID:AB 2315049
Rabbit monoclonal anti-AKT (C67E7)	Cell Signaling	Cat#4691; RRID:AB 915783
Rabbit monoclonal anti-Phospho-p44/42 MAPK (Erk1/2) (Thr202/Tyr204) (197G2)	Cell Signaling	Cat#4377; RRID:AB 331775
Rabbit monoclonal p44/42 MAPK (Erk1/2) (137F5)	Cell Signaling	Cat#4695; RRID:AB 390779
Rabbit polyclonal anti-IL6	Abcam	Cat#ab6672; RRID:AB 2127460
Rabbit polyclonal anti-pFAK (Tyr397)	Cell Signaling	Cat#3283; RRID:AB 2173659
Rabbit monoclonal anti-FAK (D2R2E)	Cell Signaling	Cat#13009; RRID:AB 2798086
Mouse monoclonal anti-PUMA α / β (G-3)	Santa Cruz Biotechnology	Cat#SC-374223; RRID:AB 10987708
Rabbit monoclonal anti-Cleaved Caspase3 (Asp175) (5A1E)	Cell Signaling	Cat#9664; RRID:AB 2070042
Mouse monoclonal anti-STEM121	Takara	Cat#Y40410; RRID:AB 2801314
Goat polyclonal anti-Factor VII	R&D systems	Cat#AF2338; RRID:AB 416580
Rabbit polyclonal anti-Lamin B1	Abcam	Cat#ab16048; RRID:AB 10107828

REAGENT or RESOURCE	SOURCE	IDENTIFIER
Rabbit polyclonal anti-phospho-GSK3 β (Ser9)	Cell signaling	Cat#9336; RRID:AB 331405
Rabbit monoclonal anti-GSK-3 β (D5C5Z)	Cell signaling	Cat# 2456; RRID:AB 2636978
Goat polyclonal anti-Hepatocyte Growth Factor	R&D systems	Cat#AF-294-NA; RRID:AB 354451
Goat polyclonal anti-Human FGF	R&D systems	Cat#AF-233-NA; RRID:AB 354413
Rabbit anti-Histone H3 (D1H2)	Cell signaling	Cat# 4499; RRID:AB 10544537
Rabbit anti-Flag Tag (D6W5B)	Cell signaling	Cat#14793; RRID:AB 2572291
Mouse monoclonal anti-F3 blocking antibody (5G9)	Absolute Antibody	Cat#ab00516 RRID:AB 2934070
Mouse monoclonal anti- α -tubulin (DM1A)	Millipore Sigma	Cat#T9026; RRID:AB 477593
Mouse monoclonal anti-actin (C-2)	Santa Cruz Biotechnology	Cat#SC-8432; RRID:AB 626630
Donkey anti-Mouse IgG (H+L) Highly Cross-Adsorbed Secondary antibody, Alexa Fluor 594	Invitrogen	Cat#A-21203; RRID:AB 141633
Donkey polyclonal anti-Mouse IgG (H+L) Cross-absorbed secondary antibody, Alexa Fluor 488	Invitrogen	Cat#A-21202; RRID: AB 141607
Donkey anti-Mouse IgG (H+L) Highly Cross-Adsorbed Secondary Antibody, Alexa Fluor™ 647	Invitrogen	Cat#A-31571; RRID: AB 162542
Donkey anti-Rabbit IgG (H+L) Highly Cross-Adsorbed Secondary antibody, Alexa Fluor 594	Invitrogen	Cat#A-21207; RRID:AB 141637
Donkey anti-Rabbit IgG (H+L) Highly Cross-absorbed secondary antibody, Alexa Fluor 488	Invitrogen	Cat#A-21206; RRID: AB 2535792
Donkey anti-Goat IgG (H+L) Cross-Adsorbed Secondary antibody, Alexa Fluor 594	Invitrogen	Cat#A-11058; RRID:AB 2534105
Donkey polyclonal anti-Goat IgG (H+L) Cross-absorbed secondary antibody, Alexa Fluor 488	Thermo Fisher Scientific	Cat#A-11055; RRID: AB 2534102
Donkey anti-Rat IgG (H+L) Highly Cross-Adsorbed Secondary antibody, Alexa Fluor 594	Invitrogen	Cat#A-21209; RRID:AB 2535795
Donkey polyclonal anti-Rat IgG (H+L) Highly Cross-Absorbed secondary antibody, Alexa Fluor 488	Thermo Fisher Scientific	Cat#A-21208; RRID: AB 2535794
Goat anti-Mouse IGG antibody (H+L), Biotinylated	Vector Laboratories	Cat#BA9200; RRID:AB 2336171
Goat anti-Rabbit IgG antibody (H+L), Biotinylated	Vector Laboratories	Cat#BA1000; RRID:AB 2313606
Goat anti-Rat IgG antibody, mouse absorbed (H+L), biotinylated	Vector Laboratories	Cat#BA9401; RRID:AB 2336208
Rabbit anti-goat IgG antibody (H+L), Biotinylated	Vector Laboratories	Cat#BA5000; RRID:AB 2336126
Biological samples		
Human glioblastoma specimen	Cleveland Clinic	
Bacterial and Virus strains		
One Shot™ Stbl3™ Chemically Competent E. coli	Thermo Fisher Scientific	C737303
Chemicals, Peptides, and Recombinant Proteins		
4% PFA	Santa Cruz Biotechnology	Cat#Sc281692; CAS: 30525-89-4
A/G agarose beads	Santa Cruz Biotechnology	SC2003
ABT-263	Selleckchem	Cat#S1001; CAS: 923564-51-6
Accutase Cell detachment solution	Sigma-Aldrich	A6964
Antigen Unmasking solution, citrate based	Vector Laboratories	H3300
B-27 Supplement (50x), minus Vitamin A	Thermo Fisher Scientific	12587010

REAGENT or RESOURCE	SOURCE	IDENTIFIER
Bafilomycin A1	Sigma-Aldrich	Cat#B1793; CAS: 88899-55-2
Blasticidin	Thermo Fisher Scientific	R21001
BLOXALL Endogenous blocking solution, peroxidase and alkaline phosphatase	Vector Laboratories	SP6000100
Bovine Serum Albumin (BSA)	Sigma-Aldrich	Cat#B6917; CAS: 9048-46-8
BYL 719	ApexBio technology	Cat#A8346; CAS: 1217486-61-7
C ₁₂ FDG (5-Dodecanoylamino fluorescein Di-β-D-Galactopyranoside)	Invitrogen	D2893
Cilengitide	Selleckchem	Cat#S6387; CAS: 188968-51-6
Cucurbitacin	Sigma-Aldrich	Cat#C4493 CAS:2222-07-3
DAPI	Sigma-Aldrich	Cat#D9542; CAS: 47165-04-8
Dasatinib	Sigma-Aldrich	Cat#SML2589; CAS: 302962-49-8
Dimethyl sulfoxide (DMSO)	Sigma-Aldrich	Cat#D2650; CAS: 67-68-5
Doxycycline	Sigma-Aldrich	Cat#D9891; CAS: 564-25-0
DMEM	Gibco	Cat#D5796
DRAQ5 fluorescent probe	Thermo Fisher Scientific	62251
Dulbecco's phosphate-buffered saline (DPBS), no calcium, no magnesium	Thermo Fisher Scientific	14190144
ECL Western Blotting detection reagents	GE Healthcare	RPN2232
Gefitinib	Abcam	Cat#ab142052; CAS: 184475-35-2
Halt Phosphatase Inhibitor Single-Use Cocktail	Thermo Fisher	78428
Lab Vison Mayer's Hematoxylin	Vector Laboratories	TA-125-MH
Lenti-X concentrator	Clontech	631231
Matrigel	Corning costar	354230
Mini Protease inhibitor cocktail	Sigma-Aldrich	11836153001
Mouse-on-mouse blocking reagent	Vector Laboratories	Cat#MKB-2213; RRID:AB 2336587
N-2 Supplement (100x)	Thermo Fisher Scientific	17502048
Neurobasal medium	Thermo Fisher Scientific	12349015
Nuclease-Free Water (not DEPC-treated)	Thermo Fisher Scientific	AM9937
O.C.T compound	SAKURA Tissue Tek	4583
Penicillin-Streptomycin	Thermo Fisher Scientific	15070063
PHA 665752	ApexBio technology	Cat#A2307; CAS: 477575-56-7
ProLong Gold Antifade Mountant	Invitrogen	P36934
Puromycin	Sigma-Aldrich	Cat#P8833; CAS:53-79-2
Saponin	Sigma-Aldrich	Cat#S7900; CAS: 8047-15-2
Sodium citrate	Sigma-Aldrich	Cat#PHR1416; CAS: 6132-04-3
Sucrose	Sigma-Aldrich	Cat#S0389; CAS: 57-50-1

REAGENT or RESOURCE	SOURCE	IDENTIFIER
Temozolomide	Sigma-Aldrich	Cat#T2577; CAS: 85622-93-1
Triton X-100	Sigma-Aldrich	Cat#T9284; CAS: 9002-93-1
Trypan blue stain, 0.4%	Thermo Fisher Scientific	T10282
VectaMount AQ Aqueous Mounting medium	Vector Laboratories	H550160
Xylene	Sigma-Aldrich	Cat#214736; CAS:1330-20-7
Critical Commercial Assays		
ATAC-Seq Library Preparation Kit	APEXBIO	K1157
CalPhos Mammalian Transfection Kit	Clontech	631312
Cell Proliferation kit (MTT)	Sigma-Aldrich	11465007001
DAB Substrate Kit	Vector Laboratories	SK4100
DNA purification Kit	Qiagen	28104
Factor 7 human chromogenic activity Assay	Abcam	ab108830
Human Cytokine antibody array kit	RayBiotech	AAH-CYT-1000
Mouse D-dimer ELISA kit	Novus Biologicals	NBP3-08100
PE Annexin V Apoptosis Detection Kit	BD biosciences	559763
QIAmp DNeasy Blood and Tissue Kit	Qiagen	69504
Senescence- β -galactosidase kit	Cell Signaling	9860
TMRE-Mitochondrial Membrane Potential Assay Kit	Abcam	ab113852
Vectastain elite ABC kit	Vector Laboratories	PK6100
CloneTracker™ 50M Lentiviral Barcode Library	Cellecta	BC13X13-V
NGS Prep Kit for Barcode Libraries in pRS116/17 (QoneTracker™)48x50ugCellectaLNGS-200	Cellecta	LNGS-200
ONE-Glo Luciferase Assay System	Promega	E6110
Deposited data		
RNA Sequencing data	This study	GEO: GSE162931
Experimental Models: Cell Lines		
NPCs from aborted fetal brain tissues	Lonza	Cat # PT-2599
Embryonic stem cell-driven NPCs	Invitrogen	Cat #N7800100
Human HEK293	ATCC	CRL-1573
Human HEK293T	ATCC	CRL-3216
Primary human astrocytes	Lonza	Cat# CC-2565
U937	ATCC	CRL-1593.2
Human glioma cells		N/A
MG63	Received from NIH	N/A
Experimental Models: Organisms/Strains		
Mouse: BALB/c, nu/nu (C.Cg/AnNTac-Foxn1 ^{nu} NE9)	TACONIC	BALBNU
Mouse: RCAS-TVA, p53 ^{-/-} , PDGFB O/E	Hambardzumyan et al. ⁵³	
Recombinant DNA		

REAGENT or RESOURCE	SOURCE	IDENTIFIER
pCMV-VSV-G	Addgene	8454
pLenti6/V5 vector	Invitrogen	K495500
psPAX2	Addgene	12260
pGreenFire 2.0 NFκB Reporter	Systems Biosciences	TR412PA-P
pGreenFire 2.0 TCF/LEF Reporter	Systems Biosciences	TR413PA-P
Software and Algorithms		
10x Genomics Chromium Single Cell Platform	10x Genomics	https://www.10xgenomics.com/products/single-cell-gene-expression
Cell ranger Pipeline	10x Genomics	https://support.10xgenomics.com/single-cell-gene-expression/software/pipelines/latest/what-is-cell-ranger
FlowJo	BD Biosciences	https://www.flowjo.com/solutions/flowjo/downloads
Gene Set Enrichment Analysis (GSEA)	Subramanian et al. ⁹³	https://www.gsea-msigdb.org/gsea/index.jsp
ImageJ	NIH	https://imagej.nih.gov/ij/
ImageScope	Leica Biosystems	https://www.leicabiosystems.com/digital-pathology/manage/aperio-imagescope/
LAS X application suite	Leica Biosystems	https://www.kica-microsystems.com/products/microscope-software/p/leica-las-x-ls/
ImageScope	Leica Biosystems	https://www.leicabiosystems.com/digital-pathology/manage/aperio-imagescope/
LAS X application suite	Leica Biosystems	https://www.kica-microsystems.com/products/microscope-software/p/leica-las-x-ls/
Plotly R package	Sievert C (2020).	https://github.com/ropensci/plotly
RayBiotech analysis tool	Raybiotech	AAH-ANG-1000
Scanpy	Wolf et al. ⁹⁴	https://scanpy.readthedocs.io/en/stable/
UMAP dimensionality reduction visualization	Becht et al. ⁹⁵	https://github.com/lmcinnes/umap
Other		
Cancer Genome Atlas (TCGA) database		
GLASS consortium		
Gene Expression Omnibus (GEO)		
Leica TCS SP5 confocal microscope	Leica Microsystems	
Zeiss EM 10 transmission electron microscope	Carl Zeiss	
Aperio AT2 Slide Scanner	Leica Microsystems	
Leica DM6B (with Leica 7000T camera)	Leica Microsystems	
LSR II Fortessa flow cytometer	BD	
FACS Aria II	BD	
Stereotactic device	Kopf instruments	
IncuCyte Live-cell analysis system	Sartorius	
Vibratome	Leica	

REAGENT or RESOURCE	SOURCE	IDENTIFIER

Author Manuscript

Author Manuscript

Author Manuscript

Author Manuscript